ROYAL SOCIETY
OF CHEMISTRY

Check for updates

Topographical characteristics of 3D printed polymeric microneedle surface and its impact on coating formulation attributes

Masood Ali,†[ab] Yanling Yang, [iD] †[a] Ayyah Abdoh[a] and Yousuf Mohammed [iD] *[ab]

In recent years, 3D printing has emerged as a promising technique for fabricating polymeric microneedles (µNDs), offering flexibility and precision. However, the surface topography of these µNDs plays a pivotal role in determining coating formulation characteristics and, consequently, their efficacy in drug delivery applications. This review delves into contemporary approaches for evaluating the surface topography of 3D printed polymeric µNDs, exploring its impact on coating formulation characteristics. With reference to the latest research in the materials industry, we elucidate the close relationship between the adhesion of coating material and µND surface, considering their physical and chemical properties. Fundamental principles relevant to understanding the influence of surface topography on therapeutic coating are discussed, emphasising how surface microtopography influences adhesion strength. Moreover, non-contact methodologies such as profilometry are reviewed for characterising µND surface morphology, highlighting their utility in assessing surface roughness, porosity, and feature geometry. Additionally, we explore how coating formulation attributes dictate surface wetting, surface energy, and interfacial adhesion strength. Insights from this review offer valuable guidance for optimising the fabrication process of 3D printed polymeric µNDs, tailoring their surface topography to enhance coating formulation performance in diverse biomedical applications.

1. Introduction

Microneedle (µND) arrays are promising biomedical devices in the transdermal drug delivery (TDD) platform. Compared to traditional injection methods, µNDs can penetrate the skin and create transient microchannels in the stratum corneum (SC), while also taking advantage of the abundant cellular network in the skin tissue. However, the temporary microchannels have been shown to close quickly. For example, Haridass *et al.* showed that after the application of Nanopatch®, a high-density µND, microchannels were closed by 25% in diameter within the first 30 min and then 100% by 6 h post-application.[1] Nonetheless, the process of inserting µND arrays into the skin causes less irritation to the subcutaneous nerves and blood vessels, and thus it is considered painless and safe.[2] A recent study quantified pain on µND treated skin using a visual analogue scale (VAS) and showed that even projections of µND longer than 1 mm caused 40% less pain than hypodermic needles.[3] In addition, due to its simple operation, the µND can be administered by the patient, which reduces the need for

trained personnel and has high patient compliance.[4] Furthermore, the advantage of bypassing the first-pass metabolism and the harsh condition of the gastrointestinal tract linked to oral administration make µNDs a useful tool for delivering therapeutics transdermally.[5]

Transdermal µNDs were originally pioneered by Mark Prausnitz's group in the late 1990s, demonstrating successful skin penetration of solid µNDs, followed by the application of a calcein-embedded patch on the prorated skin surface.[6] This two-step method "poke and patch" proved highly efficient in increasing calcein drug permeability into the skin epidermis. However, this approach is not efficient due to i) its multi-step process (create pores, then apply the drug patch) and ii) the micropores are closed after some time post microoperation, consequently limiting the diffusion of therapeutics.[5,7] To overcome these limitations, coated µNDs (CµNDs) were explored by researchers, utilising the 'coat and poke' approach.[8] CµNDs consist of solid µNDs coated with a drug-containing biocompatible material.[9] When the µND is inserted into the skin, the water-soluble coating bonded to the needle surface detaches from the projection and is dissolved in the skin, thus, delivering a wide range of active molecules, such as small molecules, viruses, DNA, and proteins.[10,11] CµNDs can only carry small doses (up to 1 mg) of drugs and are only suitable for small and potent amounts, making them widely used in vaccine research.[12–14] Several trials have shown that a microscopic level

[a] *Frazer Institute, Faculty of Medicine, University of Queensland, Brisbane, QLD 4102, Australia. E-mail: y.mohammed@uq.edu.au; Tel: +61433853534*
[b] *School of Pharmacy, The University of Queensland, Brisbane, QLD 4102, Australia*
† Co-first authors: Masood Ali and Yanling Yang.

of vaccine delivered using μNDs can successfully activate the body's immune response.[15–17] This saves a considerable amount of vaccine dose and reduces the cost and side effects of vaccination compared to vaccination by hypodermic needle injection.[12] In addition, the high storage stability of vaccines carried on μNDs reduces the reliance on cold chain storage and transportation of vaccines. It makes it highly valued in non-developed countries where resources are limited.[2,12] A major challenge encountered with CμNDs is that when μNDs are inserted into the skin, a part of the coating material remains on the skin surface and μNDs, making this part of the drug unable to enter the skin and be absorbed by the body (Fig. 1).[11]

Since then, researchers have utilised multiple approaches to overcome this issue, such as dip-coating, gas jet drying, spray coating, electrohydrodynamic atomisation (EHDA), and ink-jet printing. These methods overcome drug waste and loss, variable coating thickness, and inaccurate drug dosage.[18] These coating approaches were well documented by Haj-Ahmed *et al.*, briefly; dip-coating method involves dipping the μND into a formulation, creating a thin film over the μND surface which eventually dries into solid particles, gas-jet approach disperses a small amount of coating solution over the μND surface that removing and drying the coating solution simultaneously, spray-coating approach involves the atomisation of microdroplet formulation onto the μNDs which coalesce to form a thin film over the μNDs, EHDA coating involves producing atomised microdroplet formulation using an electrical force which is then sprayed onto the μND tips, ink-jet printing approach involves spraying a microdroplet formulation using a piezoelectric dispenser onto the μND surface for a more uniform, accurate, and reproducible coating.[19]

Researchers have also employed ink-jet printing technology to optimise coating, ejecting tiny droplets with increased control and accuracy (droplet size) on the surface of μND projection to form a uniform coating layer. Economidou *et al.* coated insulin and sugar alcohol on 3D printed μNDs using the ink-jet printing technique, forming a uniform coating with no satellite droplets falling on the μNDs substrate.[20] Uddin *et al.* reported in 2015 that ink-jet printing can coat three anticancer agents (5-fluororacil, curcumin, and cisplatin) evenly on metal μNDs.[21] In Fig. 2, Scanning Electron Microscope (SEM) analysis

demonstrated that ink-jet printing technology could precisely achieve high consistency and reproducibility for μND coating. This smoothly and uniformly coated film prevents drug loss during μND insertion, as mentioned earlier.[20]

Past studies demonstrated a correlation between surface roughness, porosity, and coating attributes.[22] In this review, we comment and extrapolate from recent literature on the relationship between topographical features and coating efficiency, as well as elucidate the relationship between surface topography and improving coating efficiency. Further, we present the most common fabrication methods and coating approaches of μNDs. We then combine the latest progress in the fields of material science and coating formulation dynamics, from the perspective of the topographical features and coating attributes of μNDs and analyse the effects of these factors on achieving uniformity in the coating of therapeutics on μND surfaces.

2. Fabrication of μNDs

μNDs fabrication techniques have been evolving ever since ALZA corporation first introduced the concept of a μND in 1976, however, it was not possible to make such micro-structured devices until the 1990s with the advent of high precision microelectronics tools.[23] Furthermore, the first paper to demonstrate μNDs technology for TDD was not until 1998, which showed a 4-fold increase in the absorption of a model drug in the human skin *in vitro*.[24] This method was, however, a poke and patch approach, where the drug diffusion is limited to the time the microchannels remain open. To alleviate that, Matriano *et al.* first reported coated silicon μND patches by immersion in a coating solution, followed by successful skin application and delivery of protein antigen for immunisation purposes.[25] Earlier CμNDs were mostly made from inorganic materials such as silicon, ceramics, and metals.[14,26] This was primarily due to the material strength and modulus needed to withstand the biomechanical strength of the skin.[26,27] It required utilising expensive instruments to optimise μND dimensional parameters such as needle geometry, size, shape, and width which depended on the skin layer depth,[23] which makes the fabrication process both costly and time

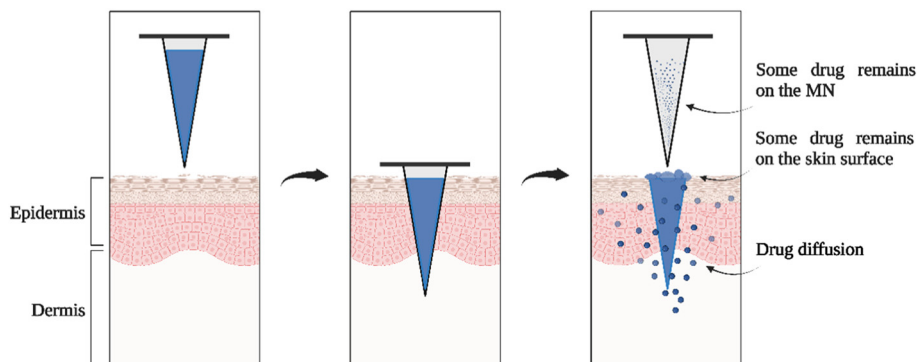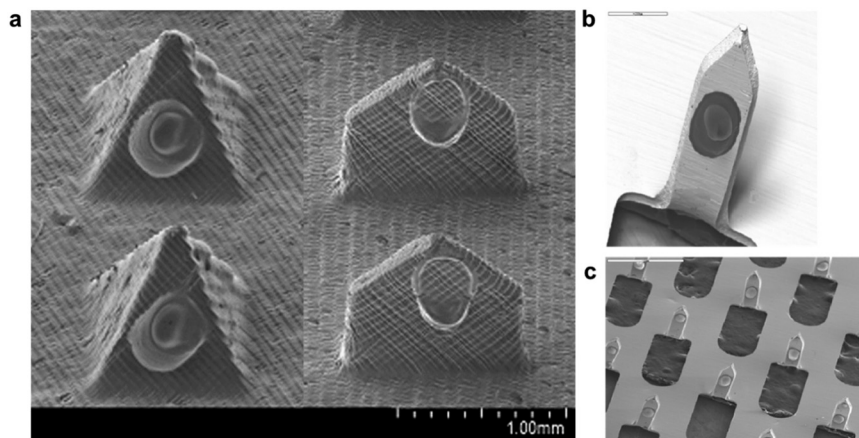**Fig. 1** Schematic illustration of methods of CμNDs application to the skin. Figure created with **https://BioRender.com** and redrawn from ref. 11.

© 2024 The Author(s). Published by the Royal Society of Chemistry

RSC Appl. Interfaces, 2024, **1**, 1108–1128 | **1109**

Fig. 2   Examples of ink-jet printed μND. (a) Coated pyramid and spear,[20] (b) and (c) μND arrays coated *via* ink-jet printing with high precision and accuracy.[21]

prohibitive.[11] Researchers have since employed low-cost and efficient fabrication techniques to manufacture μNDs, such as drawing lithography, micro-molding, and 3D printing.[28] These fabrication techniques will be highlighted in the following section. Additionally, the types of materials used, advantages and limitations of these fabrication techniques from recent studies has been highlighted in Table 1.

2.1 Lithography

Drawing lithography is the deformation of polymers by external stimuli, such as light,[41,42] centrifugal force,[43,44] electric[45,46] and magnetic fields.[29,31,47] This technique usually involves the transfer of the master pattern of geometric shapes onto a substrate surface.[29,48–51] Photolithography is the most common technique used for pattern transfer which is widely used in the field of microelectronics.[52–55] Lithography requires precise processing of the photoresist, which can be either methacrylate-based photopolymeric, photocrosslinker, or photodecomposer.[52–55] Lithography possesses the ability to create products from a variety of materials (glass, metal, ceramics, and plastics) with high geometrical precision and smooth vertical sidewalls.[29,48–55] However, this technique requires advanced cleanroom facilities[51] and extended production time.[48,54]

Table 1   Types of materials used, advantages and limitations of these fabrication methods

Method	Typical materials	Advantages	Limitations	Ref.
Lithography (electro-, thermal and magnetorheological drawing, photolithography, X-ray lithography and centrifugal)	Epoxy/novolac, thermoplastics and photo resins biocompatible polymers, ceramics	↑ Spatial resolution and consistency between batches, solid and hollow μNDs, ↑ precision	UV/X-ray curing of polymers can inactivate loaded drug, complex machinery, scale-up issues	29–33
Micromoulding	Biodegradable polymers	↑ Precision and consistency, multiple μNDs from a single mould	↑ Cost, complexity of mould design, scaling up challenges	34 and 35
Additive manufacturing: SLA, DLP, CLIP, TPP	Epoxides, acrylates, rigid (RPU) and flexible (EPU) polyurethanes, cyanate ester (CE), and prototyping (PR) resolution 100 nm–10 μm	↑ Spatial resolution (SLA < DLP < CLIP < TPP)*, built speed (TPP < SLA < DLP < CLIP), accuracy and precision (SLA < DLP < CLIP < TPP), DLP ↓ effect by oxygen inhibition	Limited materials, slow and expensive printing, SLA UV-curing of polymer matrix makes loaded drug incompatible, limited mechanical properties, CLIP requires low viscosity resin and TPP requires ↑ photon density laser	36–40
Additive manufacturing: FDM™	Thermoplastic and fiber-reinforced polymers, PLA, ABS, ASA, Nylon12, PC, PPSF/PPSU, PEI, ULTEM 50–200 μm	↓ Cost, ↑ speed and simplicity	↓ Mechanical properties, slow, rough surface, ↑ the temperature during the extrusion process, incompatible drug loading	36 and 37

N.B. for spatial resolution, the manufacturing methods are rated from least to highest convenience with regards to manufacturing process. DAB: droplet air borne, TPP: two photon polymerisation, CLIP: continuous liquid interface production, FDM: fused deposition modelling, PLA: poly(lactic acid), ABS: acrylonitrile butadiene styrene, ASA: acrylonitrile styrene acrylate, PC: polycarbonate, PPSF/PPSU: polyphenylsulfones, PEI: polyethyleneimine, ULTEM: polyetherimide.

2.2 Micromoulding

Micro-molding process consists of making replica master mould using a two-step process: first manufacturing a positive master µND array using laser[34] or lithography,[56] then using that array to fabricate replicas of negative µND mould.[57] This technique of µND fabrication is cost-effective for mass production.[34] Poly dimethyl siloxane (PDMS) is generally used to make negative micromould replicas due to its low cost, ease of use, low surface energy, and thermostability.[58–60] The limitations of this fabrication technique are the drug loading capacity and mechanical behavior of the polymer.[61]

2.3 Additive manufacturing (3D printing)

3D printing as an additive manufacturing (AM) method enables precise and reproducible fabrication of high-resolution and high-quality µNDs,[62] and can also rapidly modify the parameters associated with µNDs with the aid of computer-aided design (CAD). In addition, most 3D printing uses biocompatible polymers as raw materials, which facilitates the application of µNDs in the field of biological sciences.[62] As an efficient and inexpensive method, 3D printing is based on two classifications: material extrusion (filament-based) and photopolymerisation (resin-based). Material extrusion-based fused deposition modeling (FDM) 3D printers heat thermoplastic filament and eject it through a nozzle, where it cools and is solidified into a predetermined structure on a build platform.[63] Luzuriaga et al. printed polylactic acid (PLA) using an FDM 3D printer to create biodegradable and renewable µNDs.[64] Despite the utilisation of a large collection of thermoplastic polymers, there are disadvantages such as print layer distortion, poor surface quality, print layer thickness, width, and orientation of filament materials, which translate to dimensional inaccuracies and lower structural integrity and surface texture.[28]

Secondly, technologies such as stereolithography (SLA), digital light processing (DLP), liquid crystal display (LCD), continuous liquid interface production (CLIP), and two-photon polymerisation (TPP/2PP) are based on photopolymerisation or photocuring.[13,62,63,65] Among these technologies, structures are manufactured layer-wise using UV light to polymerise photosensitive polymers (e.g., resins). SLA is widely used due to its low cost and the high mechanical strength of the printed product.[10,66,67] Krieger et al. developed a two-step "print and fill" fabrication method for manufacturing µND master molds.[57] Unlike SLA, which uses a point light source for printing, DLP prints on the principle of printing the entire cross-section of an object at once. Therefore, even though DLP printers are very expensive, they are widely used in µND manufacturing because of their faster printing speed and high resolution.[68–71] To date, stereolithography (SLA) and digital light processing (DLP) 3D printing have been widely explored to manipulate structural changes in µNDs.[72–74] This is due to the layer-by-layer

polymerisation of UV-sensitive polymers when exposed to light with a specific wavelength (usually 350–450 nm). Xenikakis et al. printed hollow µNDs (HµND) using biocompatible resin using LCD technology.[75] As an optimised solution to traditional SLA, CLIP 3D printing has excellent printing characteristics. Caudill et al. used CLIP technology to ensure the accuracy and consistency of µND fabrication, especially producing µNDs with a smoother finish rather than a rougher finish, i.e., diminishing the 'stair-stepping' phenomenon effect on the µND surface.[76] Moreover, one study showed that CLIP technology can be used to manufacture µNDs of almost any shape in one step.[77] TPP 3D printing technology has shown the highest printing accuracy to date, enabling layer-by-layer fabrication of 3D structures at the nanoscale, and has already been commercialised.[13,78] Faraji Rad et al. used TPP technology to fabricate high-precision µND arrays with complex structures.[78] Moreover, 3D printed µNDs exhibiting dimensional variability (geometrical tweaking) possess excellent skin penetration abilities,[73,74] and this quality is very important and is required to overcome the biomechanical forces exhibited by the skin fauna during a µND penetration event.[79]

3. Topographical factors determining high fidelity µNDs

When viewed under a high-magnification microscope, the smooth surface of any material appears rough, consisting of a series of "peaks and valleys". From a micro perspective, the coating of the drug solution on µND is the adherence of the drug microparticles to the surface of the µND. The degree of adhesion of the coating material to the substrate determines the performance of the coating, and this interaction is strongly influenced by the contact topography. Also, coated films can achieve very high adhesion with rough surfaces within a certain thickness limitation.[80] After the shot peening of the substrate by Lupicka et al., the surface roughness of the substrate increased, which increased the surface area and the porosity ratio in contact between the coating material and the substrate, thus promoting the mechanical locking between them.[81,82] Surface roughness, porosity, and surface area are different physical properties of materials that are often interrelated, which will be discussed below.

3.1 Surface roughness

Surface roughness is deemed the deviation of the surface micro-features of a material from its ideal properties.[83,84] According to the relevant ISO standards, the surface roughness-related parameters include the R-system parameters in 2D and the S-system parameters in 3D. Most measurement methods assume that the roughness profile of the surface is irregular and random; therefore, the microscopic surface height of the object to be measured is often predicted to be normally distributed. Referring to ISO

© 2024 The Author(s). Published by the Royal Society of Chemistry

RSC Appl. Interfaces, 2024, 1, 1108–1128 | 1111

4287 and ISO 13565, the profile is usually described by one or more of Ra, Rz, Rq, and Rk.[84] From a computational point of view, they represent the arithmetical mean deviation of the roughness profile, the maximum height of the roughness profile, the root mean square deviation of the roughness profile, and the core roughness depth, respectively.[83,84]

Past research has shown that the topographical structure and chemical energy of a solid surface affect its wettability,[85] which represents the ability of a liquid to spread or adhere to a solid surface. Naat *et al.* investigated the improvement of surface wettability by increasing surface roughness through structured textures. The bionic textures inspired by the tree frog (TF) and fish scale (FS) lead to super-wetting of the surface and enhanced bond strength.[86] Surface wetting characteristics, including hydrophilicity and hydrophobicity, play an important role in the adhesion properties of the coatings.[87] Barreau *et al.* reported that fibrillar gecko-inspired adhesive structures can form good bonds with rough surfaces. The use of fibrillar adhesives increased the adhesion to rough substrates by a maximum of four times compared to smooth surfaces without patterns.[88] This operation of improving adhesion by modifying roughness has also been observed in studies of µNDs. Common pyramid or cone µNDs also exhibit a "stepped" microscopic appearance using high magnification SEM (Fig. 3).[57,89] This edge-ridge mismatch is a manifestation of the stair-stepping effect. Krieger *et al.* set up three print layer heights (25, 50, and 100 µm) and found that increasing the print layer height significantly reduced the surface finish, as shown in Fig. 3. This is because the edges at an angle to the *Z*-axis are rougher, making the projected surface rougher.[57]

Contact and non-contact measuring instruments are often used to measure surface roughness. The contact measurement method is based on the movement of a conical probe, usually made of diamond, over the surface of the object, obtaining topographical information about the joint profile. The stylus profilometer is a representative contact measuring instrument with low cost and high portability.[90] According to the Olympus manual, since the radius of the stylus is approximately 2 µm, when the stylus is used to measure the surface roughness of less than 2 µm, the measurement accuracy is limited, and a certain systematic error occurs. Additionally, contact measuring

instruments have the potential to damage the surface of an object during physical contact with the object. Another disadvantage of this method is that it needs to be performed in a strict measurement environment, which is difficult to operate and can only be used for off-line measurements.[91,92] Several different approaches to non-contact measurement are proposed in the literature, respectively based on ultrasound, optics, scanning tunneling microscopy (STM), and machine vision technology. Due to expensive equipment and the requirements of the measurement range and size of the test object, the application of the first three methods has been limited. On the contrary, the measurement strategy based on machine vision is favored by researchers because of its high efficiency, high precision, collection of large amounts of information, high-cost performance, and non-contact feature.[91]

3.2 Porosity

Porosity refers to the proportion of the total volume occupied by the non-solid pore space in an object. The pore morphology affects the physical properties of the material, including density, mechanical strength, and thermal conductivity.[93] According to the literature, the methods of porosity detection have been divided into two categories based on the order of processing, namely i) post-processing detection, *i.e.*, the examination of pores present in the finished object that is the most common, and ii) the inspection of pores being molded during the manufacturing process.[94]

Porosity is also an important property for applying µNDs. Porous µNDs (PµNDs) are a novel drug-loading platform with a rich microporous structure, characterised by a high surface area. Because of their unique structural features, PµNDs can utilise the capillary action generated by interconnected pores to deliver drugs and extract dermal interstitial fluid (ISF).[95] According to the scale of pore structure PµNDs have different mechanical strengths, the capacity for drug loading, and the capacity for extraction,[96] which makes them have a wide range of application besides drug delivery such as biosensing.

Many measurement methods have been developed and improved to measure porosity, such as porosimetry
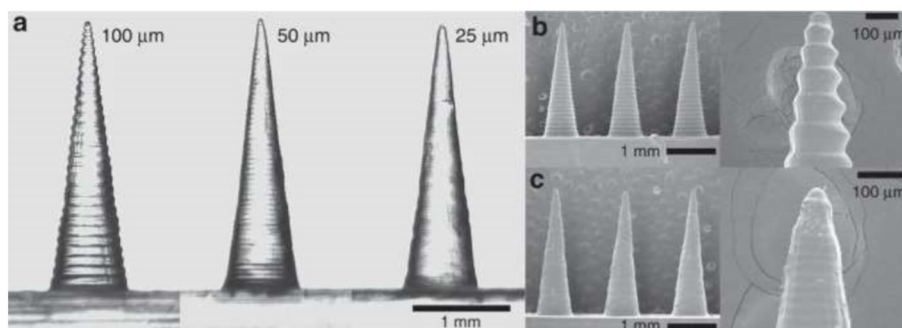
Fig. 3 Images of µNDs printed at different layer heights. (a) Comparison of 100, 50, and 25 µm layer height µNDs; (b) and (c) SEM images of 100 µm and 25 µm layer height µNDs. Image was adopted from ref. 57 with permission.

respectively based on Archimedes' principle, mercury and helium pycnometry, and lastly, image analysis methods.[93,97] Archimedeans and mercury porosimetry are widely used in science. Archimedeans porosimetry is cost-effective and convenient to operate, but it can only quantify porosity and provide limited pore information. Mercury porosimetry has high detection accuracy, but toxic high-concentration mercury residues may occur during the detection process.[93,98] Helium pycnometry measures porosity using helium gas penetrating the pores, which is highly accurate due to the high diffusivity of helium as an inert gas. But because helium gas cannot reach the closed pore regions, it can only measure the open porosity of the sample.[22] Image analysis methods are promising due to their ability to collect large amounts of data without generating toxic residues and are broadly divided into two-dimensional (2D) image analysis (optical microscopy and SEM) and three-dimensional (3D) image analysis (X-ray microtomography).[98] Table 2 lists the methods or instruments used in the research to measure the surface roughness and porosity of objects.

3.3 Surface area

The shape and size of μNDs affect the application area, mechanical strength, and drug loading amount of μNDs (Fig. 4). This correlation has been extensively covered in past publications by Coulman et al.,[112] Prausnitz et al.,[113,114] De Martino et al.,[115] Donnelly et al.,[116,117] Liu et al.,[4] Gill et al.,[11] and very recently in our publication, Ali et al.[28] These reviews have sufficiently compiled a repository of research articles
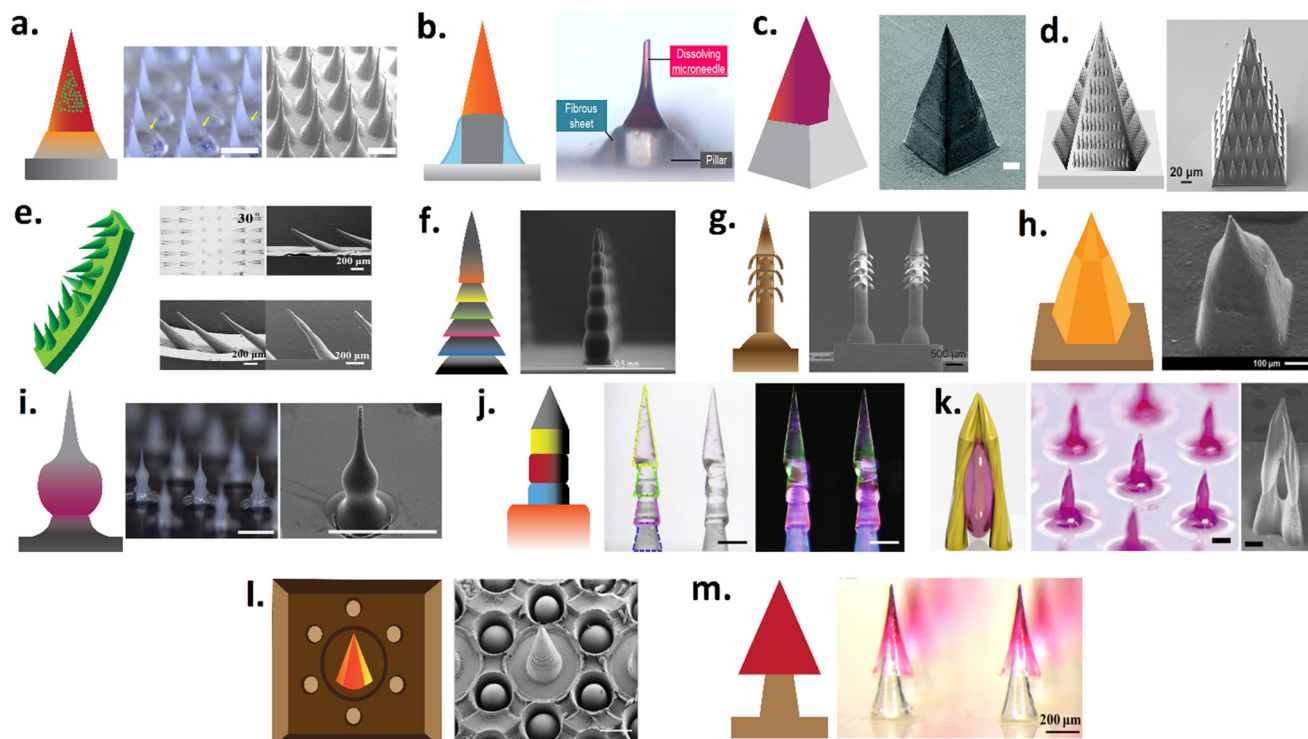
that demonstrates how different μND geometries influence the mechanical performance, skin penetration, and adhesion of coating formulations, as well as the efficiency of drug delivery systems, including the minimally invasive delivery of macromolecules and plasmid DNA. Additionally, they comprehensively review microfabrication, drug delivery mechanisms, safety considerations, material science, manufacturing processes, and the commercial development of μNDs, with a focus on the pivotal role of μND geometry in enhancing drug delivery and diagnostic applications.

The length and number of projections on the μND patches are positively correlated with their drug loading amount because of the simultaneous change in surface area. Increasing the height of the μNDs can increase the maximum load capacity by increasing the surface area, which, on the contrary, can also lead to increased pain.[77] The special projection shape may affect the drug loading efficiency more obviously.[9] To achieve high drug loading, Caudill et al. compared the surface area and drug loading of square pyramidal μND and faceted μND with horizontal grooves. The results showed that the surface area of faceted μND increased by 21.3% and drug loading increased by 36% compared with Square pyramidal μND (Fig. 4f).[76] Uddin et al. designed a cross shaped μNDs with a thousand-fold increase in coating loading (from the microgram level to the milligram level) due to the increase in surface area.[89] Li et al. systematically investigated various needle geometries of μND (cone, cone-cylinder, rectangular pyramid, and hexagonal pyramid) for the effective loading and transcutaneous delivery of ovalbumin (OVA).[129] They demonstrated that

Table 2 Methods of measuring surface roughness and porosity

Classification	Measurement methods/instrument	Advantage/disadvantages	Ref.
Contact roughness	KLA-Tensor P-15 long scan contact stylus profiler	Inexpensive and portable device	99
	Commercial scanning probe	The presence of systematic errors	100
	Tactile surface profilometer (DektakXT Stylus Profiler)	Possibility of damaging the surface	101
	Surface profilometry (Surfcorder SE 1700)	Strict measurement environment	102
		Limitations of offline measurements	
Non-contact roughness	Scanning electron microscopy (SEM) analysis	High efficiency and precision	99
	Confocal laser scanning microscopy (CLSM), Olympus LEXT OLS3100	Collection of large amounts of information	103
	White-light profilometer (ALTISURF 500)	Non-destructive technique	104
	Focus variation (FV) microscopy (Alicona InfiniteFocusSL)	Expensive equipment	105
	Talyscan-150 optical profiler (Taylor Hobson Precision Ltd)	Limitations of the measurement range and	106
	X-ray computed tomography (CT) system (Nikon Metrology MCT 225)	size of the test object	107
Archimedeans porosimetry	Measure the weight of the specimen before and after imbibition based on the Archimedes buoyancy principle	Cost-effective and easy to operate Provide limited pore information	93
Mercury porosimetry	Hg-porosimeter (Pascal 140/240 Thermo Fisher)	High detection accuracy Toxic high levels of mercury residues	108
Helium pycnometry	Micromeritics Tristar 3020 automated surface area and pore size analyser (Norcross, GA, USA)	High detection accuracy Cannot measure the closed porosity	109
	Computed micro-tomography (CMT, VersaXRM-500, Xradia, Zeiss, Jena, Germany) and helium pycnometer	High detection accuracy Measure both open and closed porosity	22
Image analysis method	Stereo and scanning electron microscopy	Collect large amounts of data	110
	Optical microscope (OM) and JEOL 7000 FEG-SEM (scanning electron microscope)	No toxic residues	102
	X-ray computed tomography (XCT) technique (Nikon Metrology 225/320 kV custom bay system)	Non-destructive technology	105
	Micro-computed tomography (microCT; Bruker AXS GmbH)	Relatively expensive equipment	111
	Using ImageJ (version 1–50) to analyse image		100

© 2024 The Author(s). Published by the Royal Society of Chemistry

RSC Appl. Interfaces, 2024, **1**, 1108–1128 | **1113**

Fig. 4 Examples of various geometrical structures of µNDs. (a) Rapidly separating µND with a bubble like structure between each µND and the patch backplate allowing for snapping off using shearing force,[118] (b) rapid implantation of dissolving µND tip into the skin by manual application (tearing through vibration), (c) square pyramidal tips designed to immediately separate from their base, which is a truncated square with a wall on one side, upon skin insertion,[119] (d) bug-inspired droplet-like structures ornamented on the lateral sides of pyramidal µND,[120] (e) serrated microstructure of mantises' forelegs inspired flexible µNDs on supporting base with clamping-like feature upon skin insertion that has rotational like movement,[121] (f) a 3D printed µND consisting of square pyramidal top and multi-faceted bottom with increased surface area for coating drugs,[76] (g) backward facing barbed of microhooks of parasites- inspired µND shaft that hooks/interlocks onto tissue upon skin insertion,[122] (h) miniature µND tip which tappers down to a wider µND body that achieves both insertion and loading of biotherapeutics,[123] (i) a tissue interlocking dissolving µNDs with a sharp tip, wide body, and narrow neck geometry,[124] (j) pagoda-like multilayered microstructure of feet or sting of an insect µND shaft for tissue fixation and interlocking,[125] (k) a microscale multi-pillar that converges to form sharp and an open cavity for drug trapping,[126] (l) inspired by mussel byssi and octopus tentacles suction-cup-structured concave chamber encircling each µND which acts as tissue adhesion cups,[127] (m) rapidly separating arrowhead dissolving µND tip mounted on a biodegradable polymer base that breaks and implants into the skin upon insertion.[128] Note, figure have been reproduced with permission from ref. 28.

conical needles exhibited structural mechanical integrity, maximum insertion efficiency (~100% of the needles inserted from one array), and a maximum *in vivo* immune response even compared to hypodermic needle-based injection. Such findings demonstrate the role of µND geometry and thus the surface area's role in the amount of drug loading and delivery.

Due to the micron size of µNDs, the loading and transdermal delivery of therapeutically relevant doses of drugs is challenging for potent therapeutics.[77] Therefore, most clinical trials involving µNDs have so far focused on the transdermal delivery of hormones and vaccines, where only microgram levels are required to produce a therapeutic response.[77] Increasing the µND height increases the surface area, thus achieving maximum drug loading, however, that can also lead to heightened pain sensation,[77] while increasing the number of µNDs in an array or patch can improve the drug loading, but it consequently increases skin puncture force due to the bed of nails effect.[130] Nonetheless, the surface area of the µNDs is an important design criterion

that dictates the amount of therapeutic drug that can be loaded.

4. µND coating methods

Although the benefit of room temperature coating may seem advantageous, the issues of insufficient therapeutic delivery have been documented due to the decreased µND sharpness as a result of coating, consequently leading to wastage and loss of delivery into the skin.[18,114] Researchers have utilised multiple approaches to overcome therapeutic wastage and loss, variable coating thickness, and inaccurate drug dosage.

Coating approaches, such as dip-coating, gas-jet drying, spray coating, electrohydrodynamic atomisation (EHDA), and ink-jet printing, have been widely explored (Fig. 5).[18,19] The simplest coating approach is the dip-coating method, which involves dipping the µND array into a drug formulation and, subsequently, creating a thin film over the µND surface, which eventually dries into solid particles coating the surface
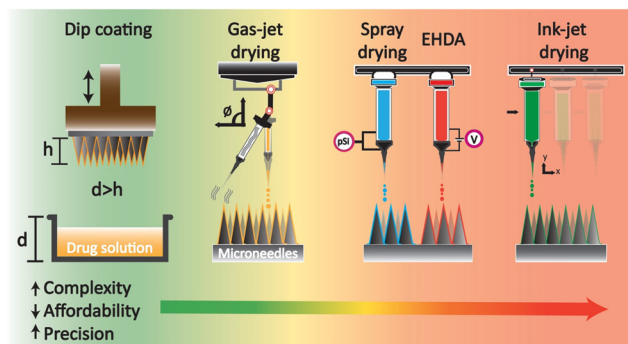
Fig. 5 Schematic illustration of drug-coated strategies on µNDs. 1) Dip coating, 2) gas-jet drying, 3) spray drying and single nozzle EHDA (while shown in the same illustration, they are separate coating strategies), and 4) single nozzle ink-jet drying. Coating strategies were redrawn from ref. 18 and 19.

of the µNDs.[11] This technique offers cost-effectiveness and simplicity but lacks uniformity and precision, leading to drug loss and potentially diminishing the ability of µNDs to penetrate the skin The gas-jet approach disperses a small amount of coating solution over the µND surface while removing and drying the coating solution simultaneously, enabling a faster drying process than dip-coating methods.[19] It allows for a faster drying process compared to dip-coating, and by adjusting the gas-jet angle, it ensures proper drying without moving the coating to the base of the µND array. However, it requires precise control of the gas-jet angle and other parameters to avoid defects. Spray coating atomises microdroplet formulations onto µNDs using fluid pressure, forming a thin film over the µNDs.[131] This technique provides more controlled and uniform coating compared to dip-coating but may require specialised equipment and fine-tuning to achieve optimal results. The EHDA coating produces an atomised microdroplet formulation using a large electrical potential difference, which is then sprayed onto the µND tips.[132] While it produces very fine and uniform droplets for coating, it involves complex instrumentation and high precision requirements. And lastly, ink-jet printing sprays microdroplet formulations using a piezoelectric dispenser onto the µND surface for a more uniform, accurate and reproducible coating.[19]

Ink-jet printing can overcome the challenges of uniform coating on the needle tips of CµNDs while ensuring the accuracy of drug dosage.[7,133] Additionally, unlike dip coating, which can produce inconsistent and copious coating, ink-jet printing has proven to produce medicated films that are relatively smooth. This smooth coating film eliminates drug loss during µND insertion into the skin.[20] Also, this avoids diminishing the ability of µNDs to penetrate the skin.[89] However, issues still persist, such as high precision requirements for instruments, unstable uniform coating, and the requirement of more than one coating cycle.[11] Despite requiring high precision instruments and possibly needing multiple coating cycles to achieve desired results, ink-jet printing is often considered superior due to its ability to

produce uniform and smooth coatings, which ensure accurate drug dosages and maintain the penetration ability of the µNDs. Its advantages in producing high-quality, reproducible coatings make it a preferred method in many applications.
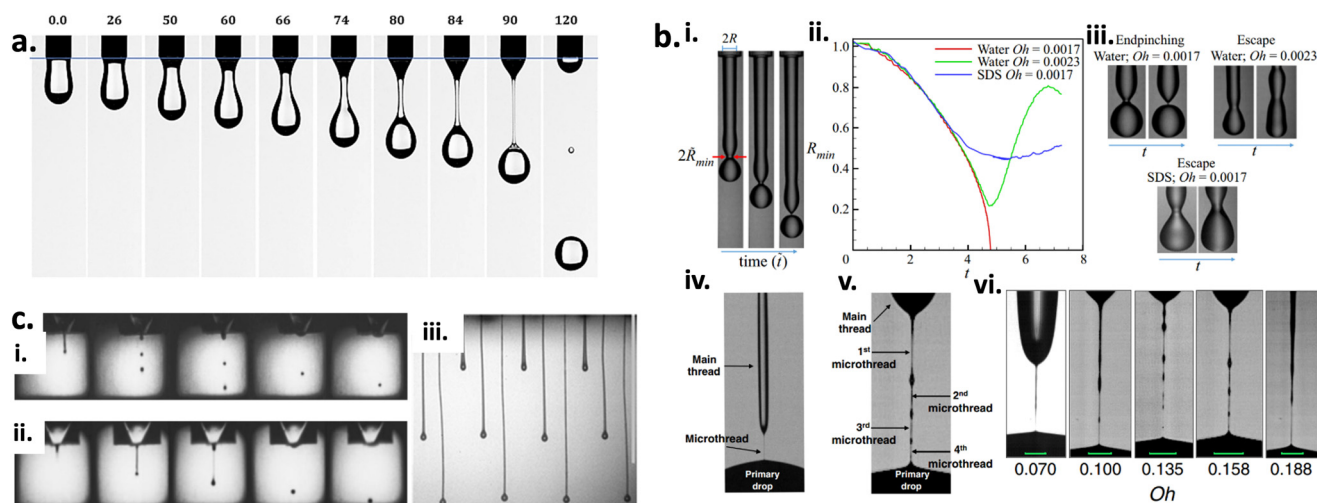
4.1 Considerations for coating formulations when using nozzle technology

Multiple analytical formulas and numerical simulations provide insights into the drop formation mechanisms in the nozzle spray technology, which is the main motive for suppressing unwanted satellite drop formation as well as controlling the properties of the jetted drop.[134] Four different drop formation methods have been identified in the literature: i) misting from the breakup of the secondary tail, ii) reproducible slow satellite droplets from pinch-off of the primary tail from the head of the drop, iii) fast reproducible satellite droplets from an initial high acceleration, and iv) Rayleigh breakup of the primary tail.[134] These factors become more complicated with the introduction of high-speed drop for Rayleigh break up of long filamentous tail of viscous fluid.[135,136] Studies using various simulation methods suggest that the underlying mechanism behind the Rayleigh breakup of long filaments lies in the onset of capillary waves.[137–139]

The main stages in the droplet formation start with the liquid ejection from the nozzle exit, stretching of the long filamentous liquid thread, pinch-off of the liquid thread from the nozzle exit, contraction of the liquid thread (capillary wave effect due to the surface tension),[139] breaking of the liquid thread in the main droplet into one or several satellites, and lastly, the recombination of the main drop with the satellite droplets (provided the satellite droplet has a higher velocity than the main droplet) (Fig. 6a).[140–145] The difference in velocity is created by the retraction of the initial thread during the pinch-off process, which is prevalent in low viscous fluid/ink,[143] as seen in Fig. 6a.[140] The filamentous thread, however, increases with the viscosity of the liquid, which consequently reduces the internal surface energy, thus drastically reducing the possibility of multiple satellite droplets from the original filamentous thread.[139] This influences the velocity and the jetting pathway of the tiny satellite droplets significantly if they experience multiple later air drag forces and can drift away from the jetting axis.[145] Therefore, to eliminate the formation of multiple satellites, passive measures are taken to reduce the lateral drag force by creating constant air current flow, and secondly, increasing the capillary energy provided by the main satellite, which, then, increases the velocity of the smaller satellites.

The main goal of the nozzle spray process is precisely controlling the droplet ejection of a minuscule amount of liquid. One way to achieve that is by adding excipients (surfactant or polymers) to control the droplet ejection from the nozzle, which consequently affects the droplet geometry.[134] Surfactants, especially, can change the inks' internal interface energies, which can lead to a complicated interaction between convection (air drying), diffusion onto the target surface, and nozzle or target surface adsorption,

© 2024 The Author(s). Published by the Royal Society of Chemistry

RSC Appl. Interfaces, 2024, **1**, 1108–1128 | **1115**

Fig. 6 (a) Demonstration graph of the droplet formation and the evolution of the neck filament of silicon oil in air. The images were captured from the movies at different time in the interval = [0, 120] ms, $v_0 = 10$ mm s^{-1}.[139] (b) Experimental results showing endpinching and escape from endpinching.[146,147] (i) Image showing the generation or formation of a filament from a nozzle and the evolution in time t of the filament's shape. In the same image, the filament at the earliest time shows twice the radius of the filament $2R$ when it exits the nozzle and twice the minimum radius of the filament's neck ($2\tilde{R}_{min}$). (ii) Variation with normalised time $vs.$ normalised minimum filament radius ($n = 3$). Red curve: water, $Oh = 0.0017$. Green curve: water, $Oh = 0.0023$. Blue curve: water plus SDS (labelled as SDS), $Oh = 0.0017$. (iii) As also shown by the images adjacent to the graph, the filament of water with $Oh = 0.0017$ endpinches whereas the other two filaments escape from endpinching. Sets of images showing the filaments at two instants in time. (iv) Endpinching: water filament with $Oh = 0.0017$ prior to and (v) at the incipience of endpinching. (vi) cluster of images showing escape (water): water filament of $Oh = 0.0023$ appearing on the cusp of breaking, and then shortly after it has escaped endpinching, while the other two images show escape (SDS): surfactant–covered filament of $Oh = 0.017$ appearing on the verge of endpinching, and then after it has undergone surfactant-driven escape from endpinching. (c) (i) Image sequence illustration from ref. 148 showing the drop formation of ink containing glycerol (50%) and water (50%) created by 50 V pulse/79 μs between frames, while (ii) shows images of drop formation for a non-Newtonian formulation (50 ppm of 300 k PEO in glycerol/water). (iii) Images showing higher polymer concentration formulations leading to the formation of long ligaments. Vertical scale bar set to 1 mm.

and all these factors determine the evolution of the final droplet geometry.[134] During the jetting process, the surfactant causes high surface tension in the droplet, which is physically measured via the oscillating droplet.[149] For non-Newtonian fluids/ink, the frequency of the oscillation is a property to measure the surface tension of the droplet, whereas the damping of the oscillation is a measure to measure the droplet viscosity (typically a time scale of 1 ms).[148,150] For most commercially available fluid/ink, measuring the oscillation frequency properties of the liquid is limited to time scales longer than 100 ms. The viscosity of the droplet is yet another important parameter to optimise to understand the behavior of the ejected droplet. Kamat et $al.$ studied the influence of surfactant (within the filamentous thread post nozzle ejection) on the pinch-off behavior of fluid/ink with both low and high viscosity.[146,147] As illustrated in Fig. 6bi–iii, for both viscous and non-viscous filamentous thread, the escape from end-pinching is driven by the action of Marangoni stress originating from the non-uniform spread of surfactant along the surface of the about-to-pinching filamentous thread. Additionally, Marangoni stresses near but not at the pinch-point give rise to the formation of multiple micro-filamentous threads (Fig. 6bv and vi), and this is different from the pinch-off of surfactant-free filamentous thread (Fig. 6biv). In other words, surfactant causes the formation of multiple micro-filamentous threads, thereby eliminating the formation of individual satellite droplets. The nozzle radius also plays an important role in filamentous thread breakage. The studies performed by Kamat et $al.$ involved nozzles with a millimeter-sized orifice. Recent studies[140,151] have shown the elimination of higher-order tails by the addition of surfactants. Additionally, higher-order tails consequently lead to the formation of femtoliter droplets, which is a pollution source.

On the other hand, the addition of long-chain macromolecular polymers can dramatically affect the breakup of filamentous threads into satellite droplets as it aids towards the viscoelasticity transforming the fluid from Newtonian fluids to non-Newtonian form.[142] The shift in states give rise to complex fluid dynamics behavior, such as shear thinning or strain hardening, either in shear-dominated or extension-dominated flows. Hoath et $al.$ reported the use of shear-thinning PEDOT: PSS polymer to suppress the formation of multiple satellite droplets.[148] This polymer solution has been shown to exhibit low viscosity upon exiting the nozzle over a range of exit/jetting speeds while rapidly recovering to a higher viscosity once the jet has formed, thus preventing multiple satellite formation. However, adding a higher concentration of polymer in the fluid/ink can lead to the formation of extremely long filamentous thread.[152] Balancing the amount of polymer added to the fluid/ink dictates the fluid dynamics of the

filamentous thread formation, which either retracts toward the droplet at the nozzle end or toward the mother droplet away from the nozzle end, as seen in Fig. 6c.[152]
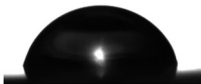
5. Coating formulation attributes

5.1 Surface wetting properties

Surface wetting is a fundamental principle crucial for achieving coating adherence on μND surfaces.[153] A reliable method for assessing substrate wetting involves measuring the contact angle between the wet coating droplet and the μND surface.[154,155] This contact angle serves as a direct indicator of the μND surface energy, defined as the angle between the liquid tangent line and the surface to be measured.[154–157] Table 3 presents the contact angle of water droplets on various commonly used polymer materials utilised in μND fabrication. A smaller contact angle suggests better wetting and, consequently, improved spreading of the coated solution onto the surface.[128]

Contact angles are typically divided into static and dynamic. Static contact angle of the coating formulation droplet on a surface determines the hydrophobicity of the contact surfaces,[128]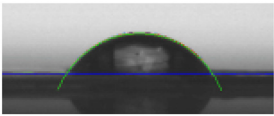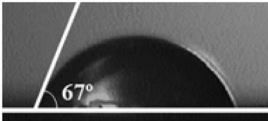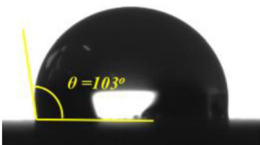 whereas dynamic contact angles are measured using the difference between the advancing θ_a and receding θ_r contact angles, respectively[166,167] (Fig. 7ai and ii), also known as the contact angle hysteresis[168,169] (Fig. 7bi and ii). Contact angle hysteresis is a fundamental principle for the adherence of coating formulation on surfaces, without which coating would not be possible on inclined surfaces.[168,169] Essentially, a lower contact angle of hysteresis is achieved on high-energy surface, which leads to better wetting and thus improved spreading of coating formulations over the surface.[166,170] Conversely, a low-energy surface results in a higher contact angle hysteresis, indicating poor wetting and thus limited spreading of the coated formulation.[166,170] Since energy (free Gibbs energy ΔG) is involved in the coating process, the coating droplet has to travel through a series of energy barriers, and as the kinetic energy of the coating droplet reduces due to the surface energy barrier, the coating droplet reaches its static wetting state, thus drying

Table 3 Contact angle of water droplet on various cured polymer solids. Images reproduced with permission from the reference in the table below

Materials	Contact angle	Water-droplet contact on the material	Ref.
Polycarbonate	70–80		158
Acrylonitrile butadiene styrene	70–80		159
Poly L-lactic acid	110–120		160
Polyurethane	70–80		161
Polystyrene	80–90		162
Polyvinyl alcohol	30–40		
Polyethylene terephthalate	50–60		163
Poly(methyl methacrylate)	60–70		164
Epoxy	103–110		165

© 2024 The Author(s). Published by the Royal Society of Chemistry

RSC Appl. Interfaces, 2024, **1**, 1108–1128 | **1117**

a. Dynamic contact angle of coating droplet on microneedle surface

i. Illustration of coating droplet showing advancing and receding angles on the surface of single microneedle

ii. Image of droplet on inclined surface and force diagram
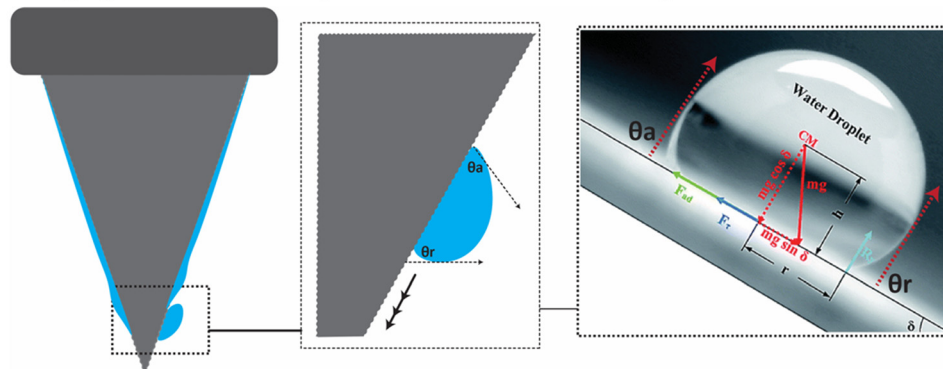
b. Contact angle hysteresis of coating formulation on spreadability

i. Illustration of relationship between contact angle (R-receding, A- advance) and Gibbs free energy (ΔG) as wetting proceeds on solid surface

ii. Relationship between surface roughness and contact angle hysteresis and spreadability
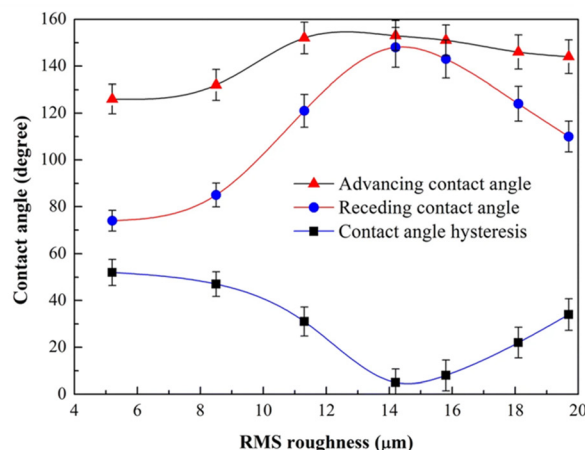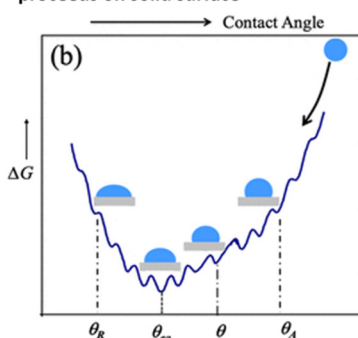
Fig. 7 Contact angle attributes of coating formulation droplet on material surface. (a) Contact angle of coating formulation droplet on inclined surface (μND) is considered as dynamic contact angle as illustrated in (i) and an image of water droplet on inclined surface (ii), illustration was redrawn from and image taken from ref. 166 and 167. (b) Relationship between the contact angle hysteresis (difference between contact angle advance and receding) of coating formulation and surface, and the coating formulation spreadability. (i) Relationship between free Gibbs energy (ΔG) of surface and the coating angle hysteresis determining spreadability, as the coating droplet moves though the surface energy barrier, the kinetic energy of coating droplet reduces thus reducing ΔG.[170] (ii) Relationship between surface roughness and contact angle hysteresis determining spreadability, the rougher the surface the lower the angle of hysteresis the better the wetting, and *vice versa*.[171]

to form a thin film (Fig. 7bi).[170] Moreover, surface energy arises from surface roughness, which also dictates the contact angle of hysteresis of the coating formulation, *i.e.*, the rougher the surface, the higher the surface energy, the lower the angle of hysteresis, the better the wetting, and *vice versa* (Fig. 7bii).[171] Therefore, contact angles of coating formulation on surfaces, and the surface energy of surfaces are related to each other, defining coating attributes such as wetting, spreadability, and adhesion. Butt *et al.* have compiled a comprehensive list of experimental techniques used to measure the contact angle of hysteresis on surface at various angles.[166]

5.2 Surface energy

The surface energy of surfaces can't be measured directly but through the contact angle of the coating formulation droplet

and, recently, through the capillary rise method.[157,172] The capillary rise method is common in dip coating of μND that uses the surface energy of the μND tip to pull the coating formulation upon contact.[157,172] As a result, a meniscus-like deformation is formed around the contact point between the μND tip and the coating solution (Fig. 8a).[172] The shape deformation occurs due to the balance of forces, surface forces (surface tension) and viscoelastic resistance. The shape of the deformation drastically changes as the drying proceeds (Fig. 8b and c),[172] *i.e.*, when the needle tip touches the coating solution, a large surface rise is formed, here the surface acts as a viscous liquid. As the drying proceeds, the deformation is concentrated near the small region of the tip, and the solvent evaporation of the coating formulation layer on the μND leads to a change from liquid phase to soft viscoelastic phase,

© 2024 The Author(s). Published by the Royal Society of Chemistry
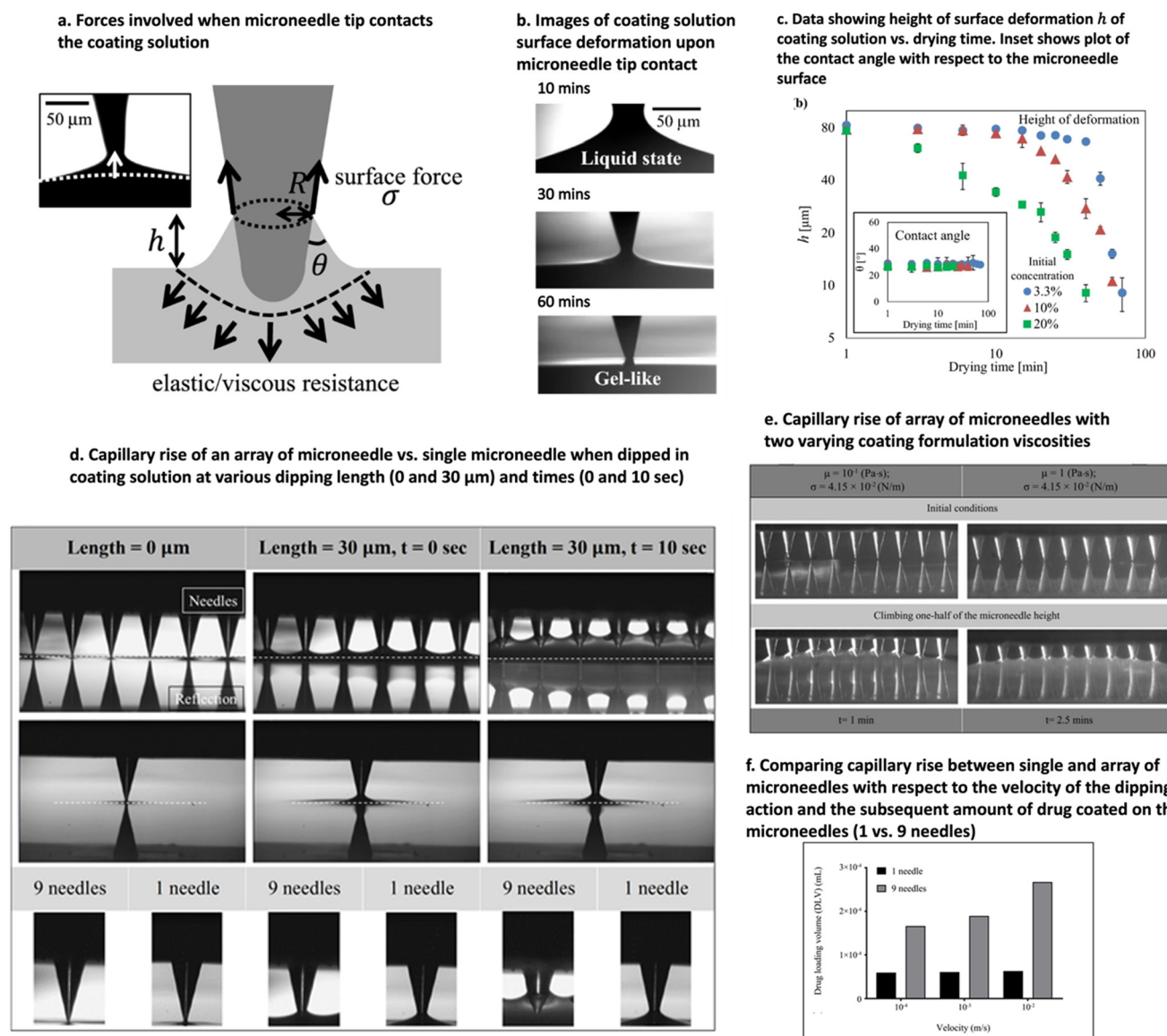
Fig. 8 Illustration of capillary rise method to measure the surface energy of the μND surface. (a) Illustration of the forces involved when μND tip touches the surface of the coating formulation. (b) Elapsed time of the μND tip touching the coating formulation from $t = 10$–30 min, showing how the viscosity of the coating formulation shape changes over time. (c) Data showing the reduction in the height 'h' of the deformation once the tip touched coating formulation surface with increasing drying time. The capillary effect of the coating formulation when the μND tip was dipped into it, showing how the speed of the dipping (d) and the viscosity of the coating formulation (e) affects the amount of drug coated on the μND tips (single *vs.* array of μND) (f). Images reproduced from ref. 157 and 172.

eventually turning into dry film with increasing finite viscoelasticity (Fig. 8b and c).[172] Additionally, Hsiao *et al.* successfully demonstrated the dip coating method of μNDs by decreasing the speed of the dipping (Fig. 8d) and increasing the viscosity of the coating solution (Fig. 8e), which increased the amount of drug coated on the surface of the μND without reaching the base of the μND (Fig. 8f).[157] Particularly the surface tension of the coating solution and the surface energy of the μND surface play a crucial role in pulling the coating formulation due to capillary action, which is dependent on the viscosity of the formulation, *i.e.*, the more viscous the coating formulation, the longer it takes to reach the base due to the reduced surface tension of the coating formulation. The

capillary rise method has proven to be quite versatile in understanding the fundamental thermodynamics of the coating process, however, further studies predicting the dynamic surface wetting and capillary interactions between each μND in an array are necessary to better predict the drug loading amount theoretically.

As mentioned previously, the adhesion force of the coating solution onto the μND surface increases with the surface energy of the μNDs.[164,173] However, it is imperative to avoid wetting the base of the μND array, as this can lead to inefficient coating and subsequent loss of drug delivery into the skin. To regulate the surface energy of μND surfaces, various surface treatment methods can be employed, including mixing 3D printed

© 2024 The Author(s). Published by the Royal Society of Chemistry

RSC Appl. Interfaces, 2024, **1**, 1108–1128 | **1119**

materials with,[174,175] surface chemical modifications,[176,177] organic polymers,[176,178] and metal oxide[176,179–181] inks. It is essential to consider that the addition of such materials to the ink may render it susceptible to organic solvents and ultraviolet light,[140] making it incompatible with traditional photolithography (Stereolithography) but suitable for nozzle technology (fused deposition model – FDM™).[141–143] Nonetheless, surface energy is a pivotal functional property that must be considered to achieve efficient adhesion of coating film layers on micro-surfaces.[164,173–186]

5.3 Interfacial adhesion strength

To achieve uniform coating on surfaces, there must be sufficient bonding strength between the coated solution and the substrate surface. One way to assess the bonding strength is by examining the adhesion properties of the coating solution. There are rheological aspects of the coating formulations that are crucial for the appropriate functioning of coating adhesion. Coating solutions must be optimised in such a manner as to enable the formation of a thin layer/film on the surface of the μNDs, which is a vital feature that can be defined through rheological tests (Fig. 9).[172,187–192] This is due to the coating solutions' viscosity properties, which exhibit viscous flow under increasing shear rates, demonstrating a shear-thinning behavior (Fig. 9a), indicating that the coating solution can be easily coated on μND surfaces, formulation can be easily injected.[172,190] However, after the coat is adhered to the μND

Fig. 9 Illustration of rheology tests used to assess the coating attributes such as: a) shear thinning curve, b) thixotropy behavior under three states (i) initially at rest with low shear rates; (ii) flow under high shear rates; (iii) recovery of coating solution at low shear rates; (c) coating hardening as a function of time, with the coating mechanism process illustrated in (d). The graphs were deduced from the following literature.[110,172,187–194]

surface (Fig. 9bii), it should recover/retain its original viscoelastic nature (microstructural rearrangement), which is known as the thixotropic phenomenon (Fig. 9biii).[172,190] Before the coating, the coating solution has an inherent viscosity (Fig. 9bi), and during the coating process, the coating solution experiences a higher mechanical strain, which results in a decrease in its viscosity (Fig. 9bii), and after the coating process, the coating solution should recover to its original viscosity (Fig. 9biii), demonstrating a thixotropic behavior.[172,190] Subsequently, once the coating film adheres to the μND site, it undergoes hardening, which is of paramount importance for coating film layer formation. This transition in the phases should be meticulously controlled, as it should not happen too quickly or too slowly (Fig. 9c).[172] Once the coating film is adhered to the μND surface, the interfacial adhesion test, specifically the peel test, can determine the strength of the adhesion to the surface.[110,193,194] The larger the strength required to peel off the coating film layer, the stronger the adhesion.[110,193,194]

5.4 Additional factors affecting coating of μND surfaces

The main topographical factors that affect coating efficiency are surface roughness, porosity, surface area and energy. Surface energy of the μND topography also complements with the surface energy of the coating solution. These interconnecting concepts aids towards understanding the behavior of coating formulation on μND surfaces, and further studies are required to have a comprehensive understanding of the μND surface coating phenomena. Thus, herein, possible considerations will be highlighted that will help researchers understand the relevant parameters in the coming years.

i. Marangoni effect. Another relevant thermocapillary phenomenon is the Marangoni effect, which promotes fluid flow at surface interfaces due to surface tension gradients resulting from temperature gradients. Slippery and lubricant-impregnated surfaces have higher surface energy thus creating temperature gradients, which them promotes the migration of coating formulation droplets out of the textured surface, leading to contact between the liquid to be repelled and the solid surface.[195] This phenomenon becomes very relevant for coating droplets containing embedded therapeutics and particles (micro/nano) movement on surfaces.[196]

ii. The interaction between droplets and solid surfaces. The interaction between droplets and solid surfaces is influenced not only by the properties of the coating formulation fluid but also by surface characteristics such as angle and chemistry. Surface roughness plays a significant role in determining droplet splashing, with factors like the splashing ratio and dynamic contact angle also contributing to this phenomenon. Moreover, chemical reactions and cross-linking can be initiated by droplet impact, presenting opportunities for conducting reactions with minimal volumes or for the controlled formation of materials. For instance, in
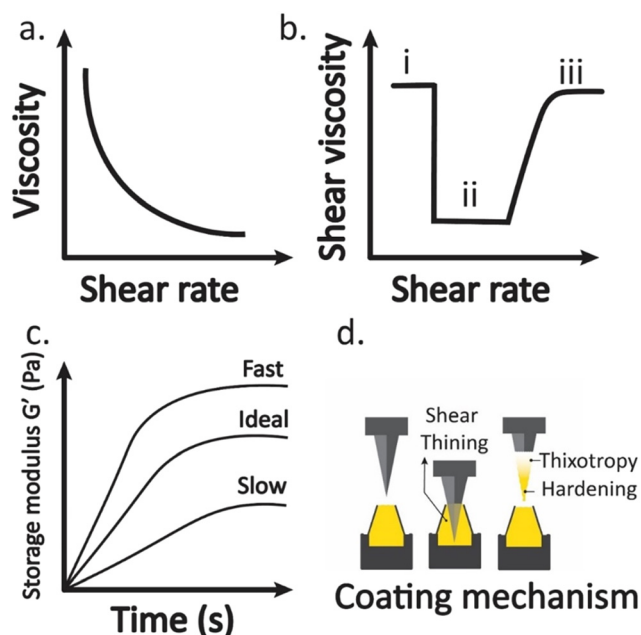
the context of natural polymeric surface coatings, compound drops, such as aqueous drops of alginate colliding with a calcium-ion-based liquid surface, can lead to the generation of complex shapes and controlled composition.[197]

iii. Impact dynamics of coating formulation on inclined surfaces. Most coating formulation droplet impact investigations focus on normal incidence (flat surface) drop impact in still air. Impact dynamic studies should also include other external forces, such as aerodynamic or tangential gravity forces respectively, as well as the tangential velocity of droplets at impact, thus breaking the axisymmetric nature of normal droplet impacts. It was not until recently, attention shifted towards the testing of such conditions, mainly due to the experimental complexity.[198–200] The complexity of testing droplet impacts rises as soon as the surface tilt angle increases, and this, consequently, increases the tangential impact velocity while reducing the normal impact velocity.[201] Additionally, the droplet consists of an inertial effect, *i.e.*, the tangential kinetic energy which is related to the gravitational effects, *i.e.*, the external force (mgsin α, whereas α is the tilting angle).[201] Proposed alternative solutions include moving the surface on rotating wheels or linearly moving surface targets.[202–204] Moreover, quantifying such parameters requires careful setting up of experimental protocols such as: i) synchronising the droplet fall with the surface motion, ii) selection of either spatial resolution or the observation window size that follows the droplet evolution post impact with the moving surface.[201] Nevertheless, such experimental setups would shed light on a wider range of impact velocities, as well as help understand the mechanism of droplet disintegration/ shedding which is promoted by external forces, such as gravity and aerodynamic drag, which overcome adhesion (capillary action) forces.[201]

iv. Air effects. Air effects have been shown to have a strong impact on the initial stages of coating formulation droplet impact onto surfaces. Droplet splashing upon impact can be suppressed by reducing the environmental pressure.[205,206] Moreover, the presence of air creates an entrapment of an air disk below the impacting droplet, as air needs to be drained from underneath the drop before the liquid can touch the surface.[207] Additionally, a recent study has demonstrated that air compressibility influenced the geometry and dynamics of this air film.[208] Future studies should examine the effect of airflow dynamics on droplets' impact close to the bottom interface of the droplet with the surface.

v. Coating uniformity. Coating uniformity is crucial in the dip coating of μNDs, wherein the capillary rise method utilises surface energy to draw coating formulations onto μND tips. This method offers flexibility in adjusting coating formulation loading by varying parameters like dipping speed and coating solution viscosity. Surface treatment methods are employed to regulate surface energy, enhancing adhesion force between the coating solution and μND surface to optimise coating efficiency and drug delivery while ensuring uniformity. Achieving uniform coating relies

on sufficient bonding strength between the coated solution and substrate surface, where rheological properties such as shear-thinning behavior and thixotropic nature play a pivotal role in proper coating formation and hardening. Interfacial adhesion tests, including peel tests, serve as valuable tools to assess the strength of adhesion between the coating film layer and the surface, ensuring optimal coating performance.

6. Conclusion

In conclusion, the integration of 3D printed μNDs with specific surface characteristics, such as roughness, surface area, and porosity, presents a promising avenue for enhancing the performance and efficacy of transdermal drug delivery systems. By carefully controlling these surface parameters, it becomes possible to modulate various aspects of the μND-skin interaction, including drug diffusion kinetics and tissue penetration efficiency. Moreover, the selection and optimisation of coating formulations play a crucial role in dictating the overall performance of coated μNDs. Attributes such as coating uniformity, contact angle, surface energy, viscosity, and surface tension significantly influence the coating process and subsequent drug release kinetics. Achieving uniform coating distribution and proper wetting properties are essential for ensuring consistent drug delivery across different skin types and application scenarios. Future research efforts should focus on further elucidating the relationships between 3D printed μND surface properties and coating formulation attributes. By gaining a deeper understanding of these interdependencies, researchers can develop more sophisticated strategies for optimising transdermal drug delivery systems, ultimately leading to enhanced therapeutic outcomes and patient experiences.

Data availability

This article is a review of existing literature, and as such, no new data were generated or analysed in this study. All data discussed are available from the original publications cited within the article.

Author contributions

Yanling Yan and Masood Ali wrote the original manuscript draft and editing. Ayyah Abdoh edited the manuscript. Yousuf Mohammed conceptualised the idea, supervised and provided support with manuscript editing and resources, submission, and management of the article.

Conflicts of interest

The authors declare that they have no known competing financial interests or personal relationships that could have appeared to influence the work reported in this paper.

© 2024 The Author(s). Published by the Royal Society of Chemistry

RSC Appl. Interfaces, 2024, **1**, 1108–1128 | 1121

Acknowledgements

References

1 I. N. Haridass, J. C. J. Wei and Y. H. Mohammed, *et al.*, Cellular metabolism and pore lifetime of human skin following microprojection array mediation, *J. Controlled Release*, 2019, **306**, 59–68.

2 A. M. Rodgers, M. T. C. McCrudden and E. M. Vincente-Perez, *et al.*, Design and characterisation of a dissolving microneedle patch for intradermal vaccination with heat-inactivated bacteria: A proof of concept study, *Int. J. Pharm.*, 2018, **549**(1), 87–95.

3 Z. Faraji Rad, P. D. Prewett and G. J. Davies, An overview of microneedle applications, materials, and fabrication methods, *Beilstein J. Nanotechnol.*, 2021, **12**, 1034–1046.

4 G.-S. Liu, Y. Kong and Y. Wang, *et al.*, Microneedles for transdermal diagnostics: Recent advances and new horizons, *Biomaterials*, 2020, **232**, 119740.

5 M. Ali, S. Namjoshi and H. A. E. Benson, *et al.*, Dissolvable polymer microneedles for drug delivery and diagnostics, *J. Controlled Release*, 2022, **347**, 561–589.

6 S. Henry, D. V. McAllister and M. G. Allen, *et al.*, Microfabricated microneedles: A novel approach to transdermal drug delivery, *J. Pharm. Sci.*, 1998, **87**(8), 922–925, DOI: **10.1021/js980042+**.

7 W. S. Shim, Y. M. Hwang and S. G. Park, *et al.*, Role of Polyvinylpyrrolidone in Dissolving Microneedle for Efficient Transdermal Drug Delivery: In vitro and Clinical Studies, *Bull. Korean Chem. Soc.*, 2018, **39**(6), 789–793, DOI: **10.1002/bkcs.11476**.

8 M. Avcil and A. Çelik, Microneedles in Drug Delivery: Progress and Challenges, *Micromachines*, 2021, **12**(11), 1321.

9 N. W. Kang, S. Kim and J. Y. Lee, *et al.*, Microneedles for drug delivery: recent advances in materials and geometry for preclinical and clinical studies, *Expert Opin. Drug Delivery*, 2021, **18**(7), 929–947.

10 S. N. Economidou, C. P. Pissinato Pere and M. Okereke, *et al.*, Optimisation of Design and Manufacturing Parameters of 3D Printed Solid Microneedles for Improved Strength, Sharpness, and Drug Delivery, *Micromachines*, 2021, **12**(2), 117.

11 R. S. J. Ingrole and H. S. Gill, Microneedle Coating Methods: A Review with a Perspective, *J. Pharmacol. Exp. Ther.*, 2019, **370**(3), 555–569.

12 I. Mansoor, H. A. Eassa and K. H. A. Mohammed, *et al.*, Microneedle-Based Vaccine Delivery: Review of an Emerging Technology, *AAPS PharmSciTech*, 2022, **23**(4), 103.

13 M. Sirbubalo, A. Tucak and K. Muhamedagic, *et al.*, 3D Printing-A "Touch-Button" Approach to Manufacture Microneedles for Transdermal Drug Delivery, *Pharmaceutics*, 2021, **13**(7), 924.

14 J. Xu, D. Xu and X. Xuan, *et al.*, Advances of Microneedles in Biomedical Applications, *Molecules*, 2021, **26**(19), 5912.

15 E. Kim, G. Erdos and S. Huang, *et al.*, Microneedle array delivered recombinant coronavirus vaccines: Immunogenicity and rapid translational development, *EBioMedicine*, 2020, **55**, 102743.

16 Y. Yin, W. Su and J. Zhang, *et al.*, Separable Microneedle Patch to Protect and Deliver DNA Nanovaccines Against COVID-19, *ACS Nano*, 2021, **15**(9), 14347–14359.

17 A. V. Boopathy, A. Mandal and D. W. Kulp, *et al.*, Enhancing humoral immunity via sustained-release implantable microneedle patch vaccination, *Proc. Natl. Acad. Sci. U. S. A.*, 2019, **116**(33), 16473–16478.

18 K. van der Maaden, W. Jiskoot and J. Bouwstra, Microneedle technologies for (trans)dermal drug and vaccine delivery, *J. Controlled Release*, 2012, **161**(2), 645–655.

19 R. Haj-Ahmad, H. Khan and M. S. Arshad, *et al.*, Microneedle Coating Techniques for Transdermal Drug Delivery, *Pharmaceutics*, 2015, **7**(4), 486–502.

20 S. N. Economidou, C. P. P. Pere and A. Reid, *et al.*, 3D printed microneedle patches using stereolithography (SLA) for intradermal insulin delivery, *Mater. Sci. Eng., C*, 2019, **102**, 743–755.

21 M. J. Uddin, N. Scoutaris and P. Klepetsanis, *et al.*, Inkjet printing of transdermal microneedles for the delivery of anticancer agents, *Int. J. Pharm.*, 2015, **494**(2), 593–602.

22 P. Cheppudira Thimmaiah, A. K. Panda and U. K. Pandey, *et al.*, A New Approach to Compute the Porosity and Surface Roughness of Porous Coated Capillary-Assisted Low Pressure Evaporators, *Sci. Rep.*, 2018, **8**(1), 11708.

23 R. F. Donnelly, T. R. Raj Singh and A. D. Woolfson, Microneedle-based drug delivery systems: microfabrication, drug delivery, and safety, *Drug Delivery*, 2010, **17**(4), 187–207.

24 S. Henry, D. V. McAllister and M. G. Allen, *et al.*, Microfabricated microneedles: a novel approach to transdermal drug delivery, *J. Pharm. Sci.*, 1998, **87**(8), 922–925.

25 J. A. Matriano, M. Cormier and J. Johnson, *et al.*, Macroflux® microprojection array patch technology: a new and efficient approach for intracutaneous immunization, *Pharm. Res.*, 2002, **19**, 63–70.

26 E. M. Cahill and E. D. O'Cearbhaill, Toward biofunctional microneedles for stimulus responsive drug delivery, *Bioconjugate Chem.*, 2015, **26**(7), 1289–1296.

27 M. Ali, S. Namjoshi and H. A. E. Benson, *et al.*, Skin biomechanics: Breaking the dermal barriers with microneedles, *Nano TransMed*, 2022, **1**(1), e9130002.

28 M. Ali, S. Namjoshi and H. A. E. Benson, *et al.*, Dissolvable polymer microneedles for drug delivery and diagnostics, *J. Controlled Release*, 2022, **347**, 561–589.

29 Z. Chen, R. Ye and J. Yang, *et al.*, Rapidly Fabricated Microneedle Arrays Using Magnetorheological Drawing Lithography for Transdermal Drug Delivery, *ACS Biomater. Sci. Eng.*, 2019, **5**(10), 5506–5513.

30 J. Jeong, J. Park and S. Lee, 3D printing fabrication process for fine control of microneedle shape, *Micro Nano Syst. Lett.*, 2023, **11**(1), 1.

31 Z. Chen, L. Ren and J. Li, *et al.*, Rapid fabrication of microneedles using magnetorheological drawing lithography, *Acta Biomater.*, 2018, **65**, 283–291.

32 H. Yang, S. Kim and G. Kang, *et al.*, Centrifugal Lithography: Self-Shaping of Polymer Microstructures Encapsulating Biopharmaceutics by Centrifuging Polymer Drops, *Adv. Healthcare Mater.*, 2017, **6**(19), 1700326.

33 H. Takahashi, Y. Jung Heo and N. Arakawa, *et al.*, Scalable fabrication of microneedle arrays via spatially controlled UV exposure, *Microsyst. Nanoeng.*, 2016, **2**(1), 16049.

34 S. L. Silvestre, D. Araújo and A. C. Marques, *et al.*, Microneedle Arrays of Polyhydroxyalkanoate by Laser-Based Micromolding Technique, *ACS Appl. Bio Mater.*, 2020, **3**(9), 5856–5864.

35 R. K. Andranilla, Q. K. Anjani and P. Hartrianti, *et al.*, Fabrication of dissolving microneedles for transdermal delivery of protein and peptide drugs: polymer materials and solvent casting micromoulding method, *Pharm. Dev. Technol.*, 2023, **28**(10), 1016–1031.

36 S. C. Ligon, R. Liska and J. Stampfl, *et al.*, Polymers for 3D Printing and Customized Additive Manufacturing, *Chem. Rev.*, 2017, **117**(15), 10212–10290.

37 T. D. Ngo, A. Kashani and G. Imbalzano, *et al.*, Additive manufacturing (3D printing): A review of materials, methods, applications and challenges, *Composites, Part B*, 2018, **143**, 172–196.

38 I. Xenikakis, M. Tzimtzimis and K. Tsongas, *et al.*, Fabrication and finite element analysis of stereolithographic 3D printed microneedles for transdermal delivery of model dyes across human skin in vitro, *Eur. J. Pharm. Sci.*, 2019, **137**, 104976.

39 R. Ali, P. Mehta and M. S. Arshad, *et al.*, Transdermal Microneedles—A Materials Perspective, *AAPS PharmSciTech*, 2019, **21**(1), 12.

40 A. Ovsianikov, B. Chichkov and P. Mente, *et al.*, Two photon polymerization of polymer-ceramic hybrid materials for transdermal drug delivery, *Int. J. Appl. Ceram. Technol.*, 2007, **4**(1), 22–29.

41 S. Liu, G. Roeder and G. Aygun, *et al.*, Simulation of 3D inclined/rotated UV lithography and its application to microneedles, *Optik*, 2012, **123**(10), 928–931.

42 Y.-K. Yoon, J.-H. Park and M. G. Allen, Multidirectional UV lithography for complex 3-D MEMS structures, *J. Microelectromech. Syst.*, 2006, **15**(5), 1121–1130.

43 H. Yang, S. Kim and G. Kang, *et al.*, Centrifugal Lithography: Self-Shaping of Polymer Microstructures Encapsulating Biopharmaceutics by Centrifuging Polymer Drops, *Adv. Healthcare Mater.*, 2017, **6**(19), 1700326.

44 S. Lee, S. Fakhraei Lahiji and J. Jang, *et al.*, Micro-Pillar Integrated Dissolving Microneedles for Enhanced Transdermal Drug Delivery, *Pharmaceutics*, 2019, **11**(8), 402.

45 F. Ruggiero, R. Vecchione and S. Bhowmick, *et al.*, Electro-drawn polymer microneedle arrays with controlled shape and dimension, *Sens. Actuators, B*, 2018, **255**, 1553–1560.

46 R. Vecchione, S. Coppola and E. Esposito, *et al.*, Electro-Drawn Drug-Loaded Biodegradable Polymer Microneedles as a Viable Route to Hypodermic Injection, *Adv. Funct. Mater.*, 2014, **24**(23), 3515–3523.

47 C. K. Choi, K. J. Lee and Y. N. Youn, *et al.*, Spatially discrete thermal drawing of biodegradable microneedles for vascular drug delivery, *Eur. J. Pharm. Biopharm.*, 2013, **83**(2), 224–233.

48 L. Cai, Z. Luo and H. Chen, *et al.*, Lithographic Microneedle-Motors from Multimodal Microfluidics for Cargo Delivery, *Small*, 2023, **19**(12), 2206108.

49 J. Y. Tan, Y. Li and F. Chamani, *et al.*, Experimental Validation of Diffraction Lithography for Fabrication of Solid Microneedles, *Materials*, 2022, **15**(24), 8934.

50 J. Y. Tan, A. Kim and J. J. Kim, Fabrication and Characterization of Hollow Microneedle Array Using Diffraction UV Lithography, *2021 21st International Conference on Solid-State Sensors, Actuators and Microsystems (Transducers)*, 2021.

51 Z. Faraji Rad, R. E. Nordon and C. J. Anthony, *et al.*, High-fidelity replication of thermoplastic microneedles with open microfluidic channels, *Microsyst. Nanoeng.*, 2017, **3**(1), 1–11.

52 H. Kathuria, K. Kang and J. Cai, *et al.*, Rapid microneedle fabrication by heating and photolithography, *Int. J. Pharm.*, 2020, **575**, 118992.

53 H. Pitakjakpipop, R. Rajan and K. Tantisantisom, *et al.*, Facile Photolithographic Fabrication of Zwitterionic Polymer Microneedles with Protein Aggregation Inhibition for Transdermal Drug Delivery, *Biomacromolecules*, 2022, **23**(1), 365–376.

54 H. Roh, Y. J. Yoon and J. S. Park, *et al.*, Fabrication of High-Density Out-of-Plane Microneedle Arrays with Various Heights and Diverse Cross-Sectional Shapes, *Nano-Micro Lett.*, 2021, **14**(1), 24.

55 Y. Han, J. Li and T. Chen, *et al.*, Modern microelectronics and microfluidics on microneedles, *Analyst*, 2023, **148**(19), 4591–4615, DOI: **10.1039/D3AN01045G**.

56 A. Malek-Khatabi, Z. Faraji Rad and M. Rad-Malekshahi, *et al.*, Development of dissolvable microneedle patches by CNC machining and micromolding for drug delivery, *Mater. Lett.*, 2023, **330**, 133328.

57 K. J. Krieger, N. Bertollo and M. Dangol, *et al.*, Simple and customizable method for fabrication of high-aspect ratio microneedle molds using low-cost 3D printing, *Microsyst. Nanoeng.*, 2019, **5**(1), 42.

58 N. Wang, Q. Wang and S. Xu, *et al.*, Mechanical Stability of PDMS-Based Micro/Nanotextured Flexible Superhydrophobic Surfaces under External Loading, *ACS Appl. Mater. Interfaces*, 2019, **11**(51), 48583–48593.

59 M. Taşdemir, F. Şenaslan and A. Çelik, Investigation of corrosion and thermal behavior of PU–PDMS-coated AISI 316L, *e-Polym.*, 2021, **21**(1), 355–365.

60 T. S. Radhakrishnan, Thermal degradation of poly(dimethylsilylene) and poly(tetramethyldisilylene-co-styrene), *J. Appl. Polym. Sci.*, 2006, **99**(5), 2679–2686.

61 M. J. Kim, S. C. Park and B. Rizal, *et al.*, Fabrication of circular obelisk-type multilayer microneedles using micro-

© 2024 The Author(s). Published by the Royal Society of Chemistry

RSC Appl. Interfaces, 2024, **1**, 1108–1128 | **1123**

milling and spray deposition, *Front. Bioeng. Biotechnol.*, 2018, **6**, 54.

62 U. Detamornrat, E. McAlister and A. R. J. Hutton, *et al.*, The Role of 3D Printing Technology in Microengineering of Microneedles, *Small*, 2022, **18**(18), 2106392.

63 S. R. Dabbagh, M. R. Sarabi and R. Rahbarghazi, *et al.*, 3D-printed microneedles in biomedical applications, *iScience*, 2021, **24**(1), 102012.

64 M. A. Luzuriaga, D. R. Berry and J. C. Reagan, *et al.*, Biodegradable 3D printed polymer microneedles for transdermal drug delivery, *Lab Chip*, 2018, **18**(8), 1223–1230, DOI: 10.1039/C8LC00098K.

65 A. Kjar and Y. Huang, Application of Micro-Scale 3D Printing in Pharmaceutics, *Pharmaceutics*, 2019, **11**(8), 390.

66 S. Choo, S. Jin and J. Jung, Fabricating High-Resolution and High-Dimensional Microneedle Mold through the Resolution Improvement of Stereolithography 3D Printing, *Pharmaceutics*, 2022, **14**(4), 766.

67 C. P. P. Pere, S. N. Economidou and G. Lall, *et al.*, 3D printed microneedles for insulin skin delivery, *Int. J. Pharm.*, 2018, **544**(2), 425–432.

68 H. Quan, T. Zhang and H. Xu, *et al.*, Photo-curing 3D printing technique and its challenges, *Bioact. Mater.*, 2020, **5**(1), 110–115.

69 E. Mathew, G. Pitzanti and A. L. Gomes Dos Santos, *et al.*, Optimization of Printing Parameters for Digital Light Processing 3D Printing of Hollow Microneedle Arrays, *Pharmaceutics*, 2021, **13**(11), 1837.

70 W. Yao, D. Li and Y. Zhao, *et al.*, 3D Printed Multi-Functional Hydrogel Microneedles Based on High-Precision Digital Light Processing, *Micromachines*, 2019, **11**(1), 17.

71 N. El-Sayed, L. Vaut and M. Schneider, Customized fast-separable microneedles prepared with the aid of 3D printing for nanoparticle delivery, *Eur. J. Pharm. Biopharm.*, 2020, **154**, 166–174.

72 A. Ovsianikov, B. Chichkov and P. Mente, *et al.*, Two photon polymerization of polymer–ceramic hybrid materials for transdermal drug delivery, *Int. J. Appl. Ceram. Technol.*, 2007, **4**(1), 22–29.

73 I. Xenikakis, M. Tzimtzimis and K. Tsongas, *et al.*, Fabrication and finite element analysis of stereolithographic 3D printed microneedles for transdermal delivery of model dyes across human skin in vitro, *Eur. J. Pharm. Sci.*, 2019, **137**, 104976.

74 A. Ovsianikov, B. Chichkov and P. Mente, *et al.*, Two Photon Polymerization of Polymer–Ceramic Hybrid Materials for Transdermal Drug Delivery, *Int. J. Appl. Ceram. Technol.*, 2007, **4**(1), 22–29.

75 I. Xenikakis, K. Tsongas and E. K. Tzimtzimis, *et al.*, Fabrication of hollow microneedles using liquid crystal display (LCD) vat polymerization 3D printing technology for transdermal macromolecular delivery, *Int. J. Pharm.*, 2021, **597**, 120303.

76 C. Caudill, J. L. Perry and K. Iliadis, *et al.*, Transdermal vaccination via 3D-printed microneedles induces potent humoral and cellular immunity, *Proc. Natl. Acad. Sci. U. S. A.*, 2021, **118**(39), e2102595118.

77 A. R. Johnson, C. L. Caudill and J. R. Tumbleston, *et al.*, Single-Step Fabrication of Computationally Designed Microneedles by Continuous Liquid Interface Production, *PLoS One*, 2016, **11**(9), e0162518.

78 Z. Faraji Rad, R. E. Nordon and C. J. Anthony, *et al.*, High-fidelity replication of thermoplastic microneedles with open microfluidic channels, *Microsyst. Nanoeng.*, 2017, **3**(1), 17034.

79 A. Masood, N. Sarika and A. E. B. Heather, *et al.*, Skin biomechanics: Breaking the dermal barriers with microneedles, *Nano TransMed*, 2022, **1**(1), e9130002.

80 S. C. L. Fischer, S. Boyadzhieva and R. Hensel, *et al.*, Adhesion and relaxation of a soft elastomer on surfaces with skin like roughness, *J. Mech. Behav. Biomed. Mater.*, 2018, **80**, 303–310.

81 K. A. Vella, J. Buhagiar and G. Cassar, *et al.*, The Effect of a Duplex Surface Treatment on the Corrosion and Tribocorrosion Characteristics of Additively Manufactured Ti-6Al-4V, *Materials*, 2023, **16**(5), 2098.

82 O. Lupicka and B. Warcholinski, The Adhesion of CrN Thin Films Deposited on Modified 42CrMo4 Steel, *Adv. Mater. Sci. Eng.*, 2017, **2017**, 4064208.

83 S. G. Croll, Surface roughness profile and its effect on coating adhesion and corrosion protection: A review, *Prog. Org. Coat.*, 2020, **148**, 105847.

84 G. Gold and K. Helmreich, A Physical Surface Roughness Model and Its Applications, *IEEE Trans. Microwave Theory Tech.*, 2017, **65**(10), 3720–3732.

85 B. Xiong, J. Li and C. He, *et al.*, Effect of pore morphology and surface roughness on wettability of porous titania films, *Mater. Res. Express*, 2020, **7**(11), 115013.

86 N. Naat, Y. Boutar and S. Naïmi, *et al.*, Influence of bio-inspired surface texture of additively manufactured 17-4 PH stainless steel adherends on the strength of adhesively bonded joints, *Int. J. Adhes. Adhes.*, 2023, **126**, 103478.

87 K. Zhou, G. Xiao and Y. Huang, Fabricating physicochemical microstructures with super hydrophilicity on Cf/SiC composites surface via picosecond-laser induced ablation, *Ceram. Int.*, 2023, **49**(21), 34291–34302.

88 V. Barreau, R. Hensel and N. K. Guimard, *et al.*, Fibrillar Elastomeric Micropatterns Create Tunable Adhesion Even to Rough Surfaces, *Adv. Funct. Mater.*, 2016, **26**(26), 4687–4694.

89 M. J. Uddin, N. Scoutaris and S. N. Economidou, *et al.*, 3D printed microneedles for anticancer therapy of skin tumours, *Mater. Sci. Eng., C*, 2020, **107**, 110248.

90 S. Liu, C. Wang and S. Du, *et al.*, 3D morphology reconstruction of rock joints from 2D profile measurement by a profilograph, *Measurement*, 2022, **203**, 112008.

91 J. Liu, E. Lu and H. Yi, *et al.*, A new surface roughness measurement method based on a color distribution statistical matrix, *Measurement*, 2017, **103**, 165–178.

92 T. Jeyapoovan and M. Murugan, Surface roughness classification using image processing, *Measurement*, 2013, **46**(7), 2065–2072.

93 Y. Zou and J. Malzbender, Development and optimization of porosity measurement techniques, *Ceram. Int.*, 2016, **42**(2, Part A), 2861–2870.

94 A. Sola and A. Nouri, Microstructural porosity in additive manufacturing: The formation and detection of pores in metal parts fabricated by powder bed fusion, *J. Adv. Manuf. Process.*, 2019, **1**(3), e10021, DOI: **10.1002/amp2.10021**.

95 E. M. Cahill, S. Keaveney and V. Stuettgen, *et al.*, Metallic microneedles with interconnected porosity: A scalable platform for biosensing and drug delivery, *Acta Biomater.*, 2018, **80**, 401–411.

96 G. Gao, L. Zhang and Z. Li, *et al.*, Porous Microneedles for Therapy and Diagnosis: Fabrication and Challenges, *ACS Biomater. Sci. Eng.*, 2023, **9**(1), 85–105.

97 F. Dullien, *Porous Media Fluid Transport and Pore Structure*, Elsevier Science, 2012.

98 Porosity Measurement in Carbon-Fiber-Reinforced Polymer Composite Through Optical Microscopy Using ImageJ Software, *Advances in Mechanical and Power Engineering*, ed. F. Monticeli, H. Voorwald and M. O. Cioffi, Springer International Publishing, Cham, 2023.

99 S. G. Croll and S. A. Payne, Quantifying abrasive-blasted surface roughness profiles using scanning electron microscopy, *J. Coat. Technol. Res.*, 2020, **17**(5), 1231–1242.

100 E. Jonda, L. Łatka and W. Pakieła, Microstructure and Selected Properties of Cr(3)C(2)-NiCr Coatings Obtained by HVOF on Magnesium Alloy Substrates, *Materials*, 2020, **13**(12), 2775.

101 M. A. Quetzeri-Santiago, A. A. Castrejón-Pita and J. R. Castrejón-Pita, The Effect of Surface Roughness on the Contact Line and Splashing Dynamics of Impacting Droplets, *Sci. Rep.*, 2019, **9**(1), 15030.

102 C. Qiu, C. Panwisawas and M. Ward, *et al.*, On the role of melt flow into the surface structure and porosity development during selective laser melting, *Acta Mater.*, 2015, **96**, 72–79.

103 J. P. B. van Dam, S. T. Abrahami and A. Yilmaz, *et al.*, Effect of surface roughness and chemistry on the adhesion and durability of a steel-epoxy adhesive interface, *Int. J. Adhes. Adhes.*, 2020, **96**, 102450.

104 S. Zouari, H. Ghorbel and C. Langlade, *et al.*, Painting Process Design and Characterization of Polymer Coatings on Brass, *J. Mater. Eng. Perform.*, 2022, **31**(1), 180–190.

105 Z. Zhu, S. Lou and C. Majewski, Characterisation and correlation of areal surface texture with processing parameters and porosity of High Speed Sintered parts, *Addit. Manuf.*, 2020, **36**, 101402.

106 K. Markandan and C. Q. Lai, Enhanced mechanical properties of 3D printed graphene-polymer composite lattices at very low graphene concentrations, *Composites, Part A*, 2020, **129**, 105726.

107 S. Carmignato, V. Aloisi and F. Medeossi, *et al.*, Influence of surface roughness on computed tomography dimensional measurements, *CIRP Ann.*, 2017, **66**(1), 499–502.

108 N. Fusi and J. Martinez-Martinez, Mercury porosimetry as a tool for improving quality of micro-CT images in low porosity carbonate rocks, *Eng. Geol.*, 2013, **166**, 272–282.

109 P. Pei, F. Yang and J. Liu, *et al.*, Composite-dissolving microneedle patches for chemotherapy and photothermal therapy in superficial tumor treatment, *Biomater. Sci.*, 2018, **6**(6), 1414–1423.

110 A. Ullah, C. M. Kim and G. M. Kim, Porous polymer coatings on metal microneedles for enhanced drug delivery, *R. Soc. Open Sci.*, 2018, **5**(4), 171609.

111 H. Vallhov, W. Xia and H. Engqvist, *et al.*, Bioceramic microneedle arrays are able to deliver OVA to dendritic cells in human skin, *J. Mater. Chem. B*, 2018, **6**(42), 6808–6816.

112 S. A. Coulman, D. Barrow and A. Anstey, *et al.*, Minimally invasive cutaneous delivery of macromolecules and plasmid DNA via microneedles, *Curr. Drug Delivery*, 2006, **3**(1), 65–75.

113 H. S. Gill and M. R. Prausnitz, Coating Formulations for Microneedles, *Pharm. Res.*, 2007, **24**(7), 1369–1380.

114 Y. C. Kim, J. H. Park and M. R. Prausnitz, Microneedles for drug and vaccine delivery, *Adv. Drug Delivery Rev.*, 2012, **64**(14), 1547–1568.

115 S. De Martino, M. Battisti and F. Napolitano, *et al.*, Effect of microneedles shape on skin penetration and transdermal drug administration, *Biomater. Adv.*, 2022, **142**, 213169.

116 R. F. Donnelly, T. R. Raj Singh and A. D. Woolfson, Microneedle-based drug delivery systems: microfabrication, drug delivery, and safety, *Drug Delivery*, 2010, **17**(4), 187–207.

117 E. Larrañeta, R. E. M. Lutton and A. D. Woolfson, *et al.*, Microneedle arrays as transdermal and intradermal drug delivery systems: Materials science, manufacture and commercial development, *Mater. Sci. Eng., R*, 2016, **104**, 1–32.

118 W. Li, J. Tang and R. N. Terry, *et al.*, Long-acting reversible contraception by effervescent microneedle patch, *Sci. Adv.*, 2019, **5**(11), eaaw8145.

119 H. Jun, M. H. Ahn and I. J. Choi, *et al.*, Immediate separation of microneedle tips from base array during skin insertion for instantaneous drug delivery, *RSC Adv.*, 2018, **8**(32), 17786–17796.

120 C. Plamadeala, S. R. Gosain and F. Hischen, *et al.*, Bio-inspired microneedle design for efficient drug/vaccine coating, *Biomed. Microdevices*, 2019, **22**(1), 8.

121 X. Zhang, F. Wang and Y. Yu, *et al.*, Bio-inspired clamping microneedle arrays from flexible ferrofluid-configured moldings, *Sci. Bull.*, 2019, **64**(15), 1110–1117.

122 D. Han, R. S. Morde and S. Mariani, *et al.*, 4D Printing of a Bioinspired Microneedle Array with Backward-Facing Barbs for Enhanced Tissue Adhesion, *Adv. Funct. Mater.*, 2020, **30**(11), 1909197.

123 J. W. Lee, S.-O. Choi and E. I. Felner, *et al.*, Dissolving Microneedle Patch for Transdermal Delivery of Human Growth Hormone, *Small*, 2011, **7**(4), 531–539.

124 J. Ohn, M. Jang and B. M. Kang, *et al.*, Dissolving Candlelit Microneedle for Chronic Inflammatory Skin Diseases, *Adv. Sci.*, 2021, **8**(14), 2004873.

125 X. Zhang, G. Chen and L. Cai, *et al.*, Bioinspired pagoda-like microneedle patches with strong fixation and hemostasis capabilities, *Chem. Eng. J.*, 2021, **414**, 128905.

126 J. Lim, D. Tahk and J. Yu, *et al.*, Design rules for a tunable merged-tip microneedle, *Microsyst. Nanoeng.*, 2018, **4**, 29–29.

127 X. Zhang, G. Chen and Y. Yu, *et al.*, Bioinspired Adhesive and Antibacterial Microneedles for Versatile Transdermal Drug Delivery, *Research.*, 2020, **2020**, 3672120.

© 2024 The Author(s). Published by the Royal Society of Chemistry

RSC Appl. Interfaces, 2024, **1**, 1108–1128 | 1125

128 D. D. Zhu, Q. L. Wang and X. B. Liu, *et al.*, Rapidly separating microneedles for transdermal drug delivery, *Acta Biomater.*, 2016, **41**, 312–319.

129 Y. Li, X. Hu and Z. Dong, *et al.*, Dissolving Microneedle Arrays with Optimized Needle Geometry for Transcutaneous Immunization, *Eur. J. Pharm. Sci.*, 2020, **151**, 105361.

130 O. Olatunji, D. B. Das and M. J. Garland, *et al.*, Influence of Array Interspacing on the Force Required for Successful Microneedle Skin Penetration: Theoretical and Practical Approaches, *J. Pharm. Sci.*, 2013, **102**(4), 1209–1221.

131 X. Ning, C. Wiraja and D. C. S. Lio, *et al.*, A Double-Layered Microneedle Platform Fabricated through Frozen Spray-Coating, *Adv. Healthcare Mater.*, 2020, **9**(10), 2000147.

132 P. Rai, N. Gautam and H. Chandra, An Experimental Approach of Generation of Micro/Nano Scale Liquid Droplets by Electrohydrodynamic Atomization (EHDA) Process, *Mater. Today: Proc.*, 2017, **4**(2, Part A), 611–620.

133 S. N. Economidou and D. Douroumis, 3D printing as a transformative tool for microneedle systems: Recent advances, manufacturing considerations and market potential, *Adv. Drug Delivery Rev.*, 2021, **173**, 60–69.

134 H. Wijshoff, Drop formation mechanisms in piezo-acoustic inkjet, *Proc Nanotech 2007*, 2007, vol. 3, p. 448.

135 A. A. Castrejón-Pita, J. R. Castrejón-Pita and I. M. Hutchings, Breakup of Liquid Filaments, *Phys. Rev. Lett.*, 2012, **108**(7), 074506.

136 J. R. Castrejón-Pita, A. A. Castrejón-Pita and S. S. Thete, *et al.*, Plethora of transitions during breakup of liquid filaments, *Proc. Natl. Acad. Sci. U. S. A.*, 2015, **112**(15), 4582–4587.

137 R. F. Day, E. J. Hinch and J. R. Lister, Self-similar capillary pinchoff of an inviscid fluid, *Phys. Rev. Lett.*, 1998, **80**(4), 704.

138 F. P. Contò, J. F. Marín and A. Antkowiak, *et al.*, Shape of a recoiling liquid filament, *Sci. Rep.*, 2019, **9**(1), 15488.

139 D. Broboana, A.-M. Bratu and I. Magos, *et al.*, Kinematics of the viscous filament during the droplet breakup in air, *Sci. Rep.*, 2022, **12**(1), 1774.

140 A. van der Bos, M.-J. van der Meulen and T. Driessen, *et al.*, Velocity profile inside piezoacoustic inkjet droplets in flight: comparison between experiment and numerical simulation, *Phys. Rev. Appl.*, 2014, **1**(1), 014004.

141 S.-H. Kang, S. Kim and D. KeeSohn, *et al.*, Analysis of drop-on-demand piezo inkjet performance, *Phys. Fluids*, 2020, **32**(2), 022007.

142 Y. Zhang, G. Hu and Y. Liu, *et al.*, Suppression and Utilization of Satellite Droplets for Inkjet Printing: A Review, *Processes*, 2022, **10**(5), 932.

143 H. Dong, W. W. Carr and J. F. Morris, An experimental study of drop-on-demand drop formation, *Phys. Fluids*, 2006, **18**(7), 072102.

144 J. Dijksman, Hydrodynamics of small tubular pumps, *J. Fluid Mech.*, 1984, **139**, 173–191.

145 E. P. Furlani, B. G. Price and G. Hawkins, *et al.*, Thermally induced Marangoni instability of liquid microjets with application to continuous inkjet printing, *Proceedings NSTI Nanotechnology Conference*, 2006.

146 P. M. Kamat, B. W. Wagoner and S. S. Thete, *et al.*, Role of Marangoni stress during breakup of surfactant-covered liquid threads: reduced rates of thinning and microthread cascades, *Phys. Rev. Fluids*, 2018, **3**(4), 043602.

147 P. M. Kamat, B. W. Wagoner and A. A. Castrejón-Pita, *et al.*, Surfactant-driven escape from endpinching during contraction of nearly inviscid filaments, *J. Fluid Mech.*, 2020, **899**, A28.

148 S. D. Hoath, W.-K. Hsiao and G. D. Martin, *et al.*, Oscillations of aqueous PEDOT: PSS fluid droplets and the properties of complex fluids in drop-on-demand inkjet printing, *J. Non-Newtonian Fluid Mech.*, 2015, **223**, 28–36.

149 H. J. Staat, A. van der Bos and M. van den Berg, *et al.*, Ultrafast imaging method to measure surface tension and viscosity of inkjet-printed droplets in flight, *Exp. Fluids*, 2017, **58**, 1–8.

150 L. Yang, B. K. Kazmierski and S. D. Hoath, *et al.*, Determination of dynamic surface tension and viscosity of non-Newtonian fluids from drop oscillations, *Phys. Fluids*, 2014, **26**(11), 113103.

151 A. Fraters, R. Jeurissen and M. van den Berg, *et al.*, Secondary tail formation and breakup in piezoacoustic inkjet printing: Femtoliter droplets captured in flight, *Phys. Rev. Appl.*, 2020, **13**(2), 024075.

152 S. D. Hoath, O. G. Harlen and I. M. Hutchings, Jetting behavior of polymer solutions in drop-on-demand inkjet printing, *J. Rheol.*, 2012, **56**(5), 1109–1127.

153 P. Zhu, R. Chen and L. Wang, Topography-Directed Hot-Water Super-Repellent Surfaces. Advanced, *Science*, 2019, **6**(18), 1900798.

154 L. Ha and J. H. Park, 3-Dimensional Coating Polymer Microneedles for Economical and Efficient Transdermal, *Drug Delivery*, 2014, **38**(3), 391–396.

155 Y. Zhu, W. Xu and Z. Cao, *et al.*, Prediction of Contact Angle for Oriented Hydrophobic Surface and Experimental Verification by Micro-Milling, *Coatings*, 2023, **13**(8), 1305.

156 V. Marturano, V. Bizzarro and V. Ambrogi, *et al.*, Light-Responsive Nanocapsule-Coated Polymer Films for Antimicrobial Active Packaging, *Polymers*, 2019, **11**, 68.

157 H.-F. Y. Meng-Hsuan Hsiao, T.-J. Liu and J. Wang, Drug Loading on Microneedles [Research article], *Adv. Chem. Eng. Sci.*, 2019, **9**(2), 204–222.

158 P. S. Brown and B. Bhushan, Durable, superoleophobic polymer–nanoparticle composite surfaces with re-entrant geometry via solvent-induced phase transformation, *Sci. Rep.*, 2016, **6**(1), 21048.

159 N. H. Che Ismail and H. Md. Akil, Effects of organomodified muscovite on the properties of acrylonitrile–butadiene–styrene nanocomposites, *J. Appl. Polym. Sci.*, 2018, **135**(47), 46827.

160 E. Thangaraju, N. T. Srinivasan and R. Kumar, *et al.*, Fabrication of electrospun Poly L-lactide and Curcumin loaded Poly L-lactide nanofibers for drug delivery, *Fibers Polym.*, 2012, **13**(7), 823–830.

161 S. Y. Lee, Y. Lee and P. Le Thi, *et al.*, Sulfobetaine methacrylate hydrogel-coated anti-fouling surfaces for

implantable biomedical devices, *Biomater. Res.*, 2018, **22**(1), 3.

162 P. Muanchan, T. Kurose and H. Ito, Replication of Mesoscale Pore One-dimensional Nanostructures: Surface-induced Phase Separation of Polystyrene/Poly(vinyl alcohol) (PS/PVA) Blends, *Polymers*, 2019, **11**(6), 1039.

163 C.-S. Park, E. Y. Jung and H. J. Jang, *et al.*, Synthesis and Properties of Plasma-Polymerized Methyl Methacrylate via the Atmospheric Pressure Plasma Polymerization Technique, *Polymers*, 2019, **11**(3), 396.

164 K. Tokuda, T. Ogino and M. Kotera, *et al.*, Simple method for lowering poly(methyl methacrylate) surface energy with fluorination, *Polym. J.*, 2015, **47**(1), 66–70.

165 W. Shang and H. Jiang, Preparation and properties of a novel fluorinated epoxy resin/DGEBA blend for application in electronic materials, *High Perform. Polym.*, 2020, **32**(7), 793–800.

166 H.-J. Butt, J. Liu and K. Koynov, *et al.*, Contact angle hysteresis, *Curr. Opin. Colloid Interface Sci.*, 2022, **59**, 101574.

167 B. S. Yilbas, A. Al-Sharafi and H. Ali, *et al.*, Dynamics of a water droplet on a hydrophobic inclined surface: influence of droplet size and surface inclination angle on droplet rolling, *RSC Adv.*, 2017, **7**(77), 48806–48818.

168 A. Pockels, Über Randwinkel und Ausbreitung von Flüssigkeiten auf festen Körpern, *Phys. Z.*, 1914, **15**, 39–46.

169 H. B. Eral, D. t Mannetje and J. M. Oh, Contact angle hysteresis: a review of fundamentals and applications, *Colloid Polym. Sci.*, 2013, **291**, 247–260.

170 K.-Y. Law, Contact Angle Hysteresis on Smooth/Flat and Rough Surfaces. Interpretation, Mechanism, and Origin, *Acc. Mater. Res.*, 2022, **3**(1), 1–7.

171 J. Wang, Y. Wu and Y. Cao, *et al.*, Influence of surface roughness on contact angle hysteresis and spreading work, *Colloid Polym. Sci.*, 2020, **298**(8), 1107–1112.

172 T. Kajiya, D. Sawai and K. Miyata, *et al.*, Simple method to measure rheological properties of soft surfaces by a micro-needle contact, *Eur. Phys. J. E: Soft Matter Biol. Phys.*, 2022, **45**(9), 76.

173 B. Cabanillas, A. Mallma-Medina and M. Petkova-Gueorguieva, *et al.*, Influence of the Surface Energy of Different Brands of Polymethyl Methacrylate on the Adherence of Candida albicans: An In Vitro Study, *J. Int. Soc. Prev. Community Dent.*, 2021, **11**(1), 6–12.

174 A. Mazzotta, A. Gabbani and M. Carlotti, *et al.*, Invisible Thermoplasmonic Indium Tin Oxide Nanoparticle Ink for Anti-counterfeiting Applications, *ACS Appl. Mater. Interfaces*, 2022, **14**(30), 35276–35286.

175 K. Parate, S. V. Rangnekar and D. Jing, *et al.*, Aerosol-Jet-Printed Graphene Immunosensor for Label-Free Cytokine Monitoring in Serum, *ACS Appl. Mater. Interfaces*, 2020, **12**(7), 8592–8603.

176 M. Borghetti, M. Serpelloni and E. Sardini, *et al.*, Mechanical behavior of strain sensors based on PEDOT:PSS and silver nanoparticles inks deposited on polymer substrate by inkjet printing, *Sens. Actuators, A*, 2016, **243**, 71–80.

177 J. Lee, J. Kim and J. Park, *et al.*, Characterization of in situ sintering of silver nanoparticles on commercial photo papers in inkjet printing, *Flexible Printed Electron.*, 2018, **3**(2), 025001.

178 D. Lv, W. Chen and W. Shen, *et al.*, Enhanced flexible room temperature ammonia sensor based on PEDOT: PSS thin film with FeCl3 additives prepared by inkjet printing, *Sens. Actuators, B*, 2019, **298**, 126890.

179 M. Shariq, S. Chattopadhyaya and R. Rudolf, *et al.*, Characterization of AuNPs based ink for inkjet printing of low cost paper based sensors, *Mater. Lett.*, 2020, **264**, 127332.

180 D. M. Stanković, M. Ognjanović and M. Jović, *et al.*, Disposable Biosensor Based on Amidase/CeO2/GNR Modified Inkjet-printed CNT Electrodes-droplet Based Paracetamol Detection in Biological Fluids for "Point-of-care" Applications, *Electroanalysis*, 2019, **31**(8), 1517–1525.

181 D. Bugakova, V. Slabov and E. Sergeeva, *et al.*, Comprehensive characterization of TiO2 inks and their application for inkjet printing of microstructures, *Colloids Surf., A*, 2020, **586**, 124146.

182 A. Kowalski and Z. Czech, The effects of substrate surface properties on tack performance of acrylic Pressure-Sensitive Adhesives (PSAs), *Int. J. Adhes. Adhes.*, 2015, **60**, 9–15.

183 S. Wang, J. Xu and W. Wang, *et al.*, Skin electronics from scalable fabrication of an intrinsically stretchable transistor array, *Nature*, 2018, **555**(7694), 83–88.

184 M. J. Kim, S. C. Park and S.-O. Choi, Dual-nozzle spray deposition process for improving the stability of proteins in polymer microneedles, *RSC Adv.*, 2017, **7**(87), 55350–55359, DOI: **10.1039/C7RA10928H**.

185 U. Angkawinitwong, A. J. Courtenay and A. M. Rodgers, *et al.*, A Novel Transdermal Protein Delivery Strategy via Electrohydrodynamic Coating of PLGA Microparticles onto Microneedles, *ACS Appl. Mater. Interfaces*, 2020, **12**(11), 12478–12488.

186 C. O'Mahony, A. Bocchino and M. J. Haslinger, *et al.*, Piezoelectric inkjet coating of injection moulded, reservoir-tipped microneedle arrays for transdermal delivery, *J. Micromech. Microeng.*, 2019, **29**(8), 085004.

187 S. Bakshi, P. Pandey and Y. Mohammed, *et al.*, Porous silicon embedded in a thermoresponsive hydrogel for intranasal delivery of lipophilic drugs to treat rhinosinusitis, *J. Controlled Release*, 2023, **363**, 452–463.

188 X. Jin, S. E. Alavi and A. Shafiee, *et al.*, Metamorphosis of Topical Semisolid Products—Understanding the Role of Rheological Properties in Drug Permeation under the "in Use" Condition, *Pharmaceutics*, 2023, **15**(6), 1707.

189 M. Dabbaghi, S. Namjoshi and B. Panchal, *et al.*, Viscoelastic and Deformation Characteristics of Structurally Different Commercial Topical Systems, *Pharmaceutics*, 2021, **13**(9), 1351.

190 E. E. Peters, M. Ameri and X. Wang, *et al.*, Erythropoietin-Coated ZP-Microneedle Transdermal System: Preclinical Formulation, Stability, and Delivery, *Pharm. Res.*, 2012, **29**(6), 1618–1626.

191 H. Kathuria, D. Lim and J. Cai, *et al.*, Microneedles with Tunable Dissolution Rate, *ACS Biomater. Sci. Eng.*, 2020, **6**(9), 5061–5068.

© 2024 The Author(s). Published by the Royal Society of Chemistry

RSC Appl. Interfaces, 2024, **1**, 1108–1128 | **1127**

192 Q. Jing, H. Ruan and J. Li, et al., Keratinocyte membrane-mediated nanodelivery system with dissolving microneedles for targeted therapy of skin diseases, Biomaterials, 2021, 278, 121142.

193 S. W. T. Chew, A. H. Shah and M. Zheng, et al., A self-adhesive microneedle patch with drug loading capability through swelling effect, Bioeng. Transl. Med., 2020, 5(2), e10157.

194 Z. Zhu, J. Wang and X. Pei, et al., Blue-ringed octopus-inspired microneedle patch for robust tissue surface adhesion and active injection drug delivery, Sci. Adv., 2023, 9(25), eadh2213.

195 N. Bjelobrk, H.-L. Girard and S. B. Subramanyam, et al., Thermocapillary motion on lubricant-impregnated surfaces, Phys. Rev. Fluids, 2016, 1(6), 063902.

196 J. B. Brzoska, F. Brochard-Wyart and F. Rondelez, Motions of droplets on hydrophobic model surfaces induced by thermal gradients, Langmuir, 1993, 9(8), 2220–2224.

197 E. Mele, D. Fragouli and R. Ruffilli, et al., Complex architectures formed by alginate drops floating on liquid surfaces, Soft Matter, 2013, 9(27), 6338–6343.

198 J. Hao, J. Lu and L. Lee, et al., Droplet splashing on an inclined surface, Phys. Rev. Lett., 2019, 122(5), 054501.

199 J. Hao, J. Lu and Z. Zhang, et al., Asymmetric droplet splashing, Phys. Rev. Fluids, 2020, 5(7), 073603.

200 P. García-Geijo, G. Riboux and J. M. Gordillo, Inclined impact of drops, J. Fluid Mech., 2020, 897, A12.

201 N. Blanken, M. S. Saleem and M.-J. Thoraval, et al., Impact of compound drops: a perspective, Curr. Opin. Colloid Interface Sci., 2021, 51, 101389.

202 J. Hao and S. I. Green, Splash threshold of a droplet impacting a moving substrate, Phys. Fluids, 2017, 29(1), 012103.

203 H. Almohammadi and A. Amirfazli, Understanding the drop impact on moving hydrophilic and hydrophobic surfaces, Soft Matter, 2017, 13(10), 2040–2053.

204 S. Buksh, H. Almohammadi and M. Marengo, et al., Spreading of low-viscous liquids on a stationary and a moving surface, Exp. Fluids, 2019, 60, 1–12.

205 D. A. Burzynski and S. E. Bansmer, Role of surrounding gas in the outcome of droplet splashing, Phys. Rev. Fluids, 2019, 4(7), 073601.

206 Z. Jian, C. Josserand and S. Popinet, et al., Two mechanisms of droplet splashing on a solid substrate, J. Fluid Mech., 2018, 835, 1065–1086.

207 C. Josserand and S. T. Thoroddsen, Drop impact on a solid surface, Annu. Rev. Fluid Mech., 2016, 48, 365–391.

208 E. Li and S. T. Thoroddsen, Time-resolved imaging of a compressible air disc under a drop impacting on a solid surface, J. Fluid Mech., 2015, 780, 636–648.